Geochemistry, Geophysics, Geosystems®

AGU ADVANCING EARTH AND SPACE SCIENCES

RESEARCH ARTICLE
10.1029/2023GC011174

Key Points:

- Ocean bottom seismometers allowed improved seismicity imaging in the eastern Fram Strait
- Integration of earthquakes and seismic data revealed a buried spreading center at the Molloy Transform Fault—Knipovich Ridge intersection
- Two earthquakes at a zone of sedimentary faulting and active seepage at the Vestnesa Ridge, suggesting accommodation of crustal faults

Supporting Information:

Supporting Information may be found in the online version of this article.

Correspondence to:

P. Domel,
przemyslaw.domel@uit.no

Citation:

Domel, P., Plaza-Faverola, A., Schlindwein, V., & Bünz, S. (2023). Local seismicity and sediment deformation in the west Svalbard margin: Implications of neotectonics for seafloor seepage. *Geochemistry, Geophysics, Geosystems*, *24*, e2023GC011174. https://doi.org/10.1029/2023GC011174

Received 14 AUG 2023
Accepted 20 NOV 2023

Local Seismicity and Sediment Deformation in the West Svalbard Margin: Implications of Neotectonics for Seafloor Seepage

P. Domel[1], A. Plaza-Faverola[2], V. Schlindwein[3,4], and S. Bünz[2]

[1]Department of Geosciences, UiT—The Arctic University of Norway, Tromsø, Norway, [2]iC3: Centre for ice, Cryosphere, Carbon and Climate, Department of Geosciences, UiT—The Arctic University of Norway, Tromsø, Norway, [3]Alfred Wegener Institute, Helmholtz Centre for Polar and Marine Research, Bremerhaven, Germany, [4]Faculty of Geosciences, University of Bremen, Bremen, Germany

Abstract In the Fram Strait, mid-ocean ridge spreading is represented by the ultra-slow system of the Molloy Ridge, the Molloy Transform Fault and the Knipovich Ridge. Sediments on oceanic and continental crust are gas charged and there are several locations with documented seafloor seepage. Sedimentary faulting shows recent stress release in the sub-surface, but the drivers of stress change and its influence on fluid flow are not entirely understood. We present here the results of an 11-month-long ocean bottom seismometer survey conducted over the highly faulted sediment drift northwards from the Knipovich Ridge to monitor seismicity and infer the regional state of stress. We obtain a detailed earthquake catalog that improves the spatial resolution of mid-ocean ridge seismicity compared with published data. Seismicity at the Molloy Transform Fault is occurring southwards from the bathymetric imprint of the fault, as supported by a seismic profile. Earthquakes in the northern termination of the Knipovich Ridge extend eastwards from the ridge valley, which together with syn-rift faulting identified in seismic reflection data, suggests that a portion of the currently active spreading center is buried under sediments away from the bathymetric expression of the rift valley. This hints at the direct link between crustal rifting processes and faulting in shallow sediments. Two earthquakes occur close to the seepage system of the Vestnesa Ridge further north from the network. We suggest that deeper rift structures, reactivated by gravity and/or post-glacial subsidence, may lead to accommodation of stress through shallow extensional faults, therefore impacting seepage dynamics.

Plain Language Summary In the Fram Strait, between Greenland and Svalbard, the ocean floor is slowly spreading due to the plate motion and this process generates most of the seismicity in the region and is also responsible for sediment faulting. In this area, sediments are known to contain gas accumulations and gas is being released into the ocean. It is still not well understood whether sediment deformation and gas release are controlled by the plate motion and crustal changes following deglaciation of the continents. To capture weak seismicity, it is necessary to have seismometers deployed locally on the ocean floor. This study uses the data from a network of ocean bottom seismometers, which were placed at the seafloor and recorded seismicity for 11 months. Local seismicity and high-resolution seismic data show regions of present-day tectonic deformation and help to better identify major active faults in the rift valley. At the Molloy Transform Fault, earthquakes occur further south than expected, and the seismic line shows shallow sediment faulting. Our results suggest that thick sediment deposits adjacent to the mid-ocean ridges may reactivate deep rift structures and accommodate stress through extensional faults that leaked methane over geological time.

1. Introduction

Sedimentary structures in ocean margin settings are controlled by the local stress field. This field is influenced by external (e.g., tectonic, glaciotectonic) and internal factors (e.g., pore fluid pressure). Constraining the forces exerted on the sedimentary column along continental margins is crucial to understand seismicity, fault development, structural deformation, and fluid transfer to the ocean (e.g., England et al., 1987; Judd & Hovland, 2007). This knowledge is important in the risk assessment of tsunami hazard and landslide generation with implications on both submarine (e.g., fiber telecommunication cables) and coastal infrastructures (e.g., Carter et al., 2014; Gardner et al., 2001). It also improves our understanding of natural hydrocarbon seepage (e.g., Etiope, 2015), and aids in risk assessment of potential carbon capture and storage projects (e.g., Solomon et al., 2008).

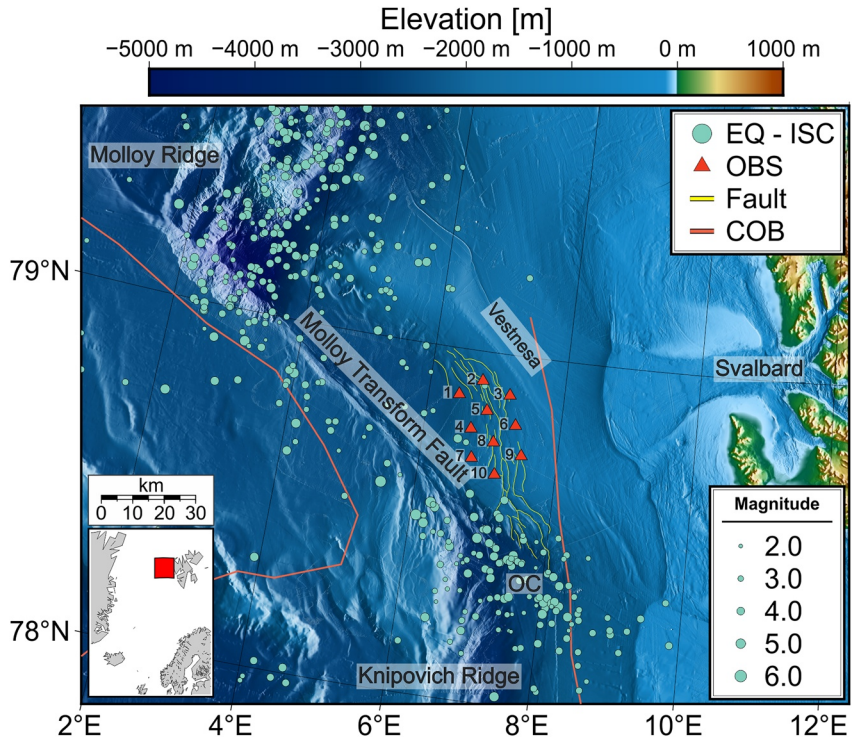

Figure 1. Overview map of the area investigated in this study. Red triangles represent the position of deployed ocean bottom seismometers over the investigated fault structures (yellow lines). Circles represent earthquake locations for the area provided by the International Seismological Center (ISC) for years between 1960 and 2020. Orange lines outline the most recent estimates of continent-ocean crust boundary (COB in the legend; Dumais et al., 2021). One of the areas of interest discussed later—the outside corner between the Molloy Transform Fault and the Knipovich Ridge labeled as OC. Bathymetry provided by the International Bathymetric Chart of the Arctic Ocean (IBCAO).

As its name implies, "passive" margins are classically considered to be inactive, with no plate tectonic influence on the present-day change in the stress field (indicated by seismological activity) away from the spreading ridge zones or transform faults (Miall, 2013). It is generally assumed that deformation within the sedimentary cover along rifted margins is related to gravitational processes such as sliding, slumping, listric faulting, mud diapirism, focused fluid flux, and potentially salt tectonics (Allen & Allen, 2013). However, recent observations at divergent continental margins (e.g., along the N and S Atlantic Ocean), indicate that the assumption of tectonic quiescence of these regions during the post-rift phase does not match observations in seismic profiles and heat flow measurements (Paton, 2011). Some passive margins remain in structural balance over long periods of time until small changes in the overall conditions drive them into instability (Hudec & Jackson, 2004). The mechanisms driving changes in the local stress field in shallow sediments remain poorly understood.

Several factors contribute to the local state of stress. Plate tectonics is one of the major forces behind the current stress regime in the lithosphere (Zoback et al., 1989). In the Arctic Ocean, plate tectonics is associated with mid-ocean ridge spreading, which is responsible for the majority of the seismological activity observed in the region. In the Fram Strait, between Greenland and Svalbard, the ridge system consists of the Molloy Ridge (MR) and the Knipovich Ridge (KR), connected by the Molloy Transform Fault (MTF) (e.g., Crane et al., 1991; Figure 1). The MR is connected to the Gakkel Ridge in the north and the KR to the Mohns Ridge in the south. Both the MR and KR are classified as ultra-slow spreading systems (Dick et al., 2003). Spreading rates at the MR are about 6.5 mm/y for the western side and 6.3 mm/y for the eastern part (Ehlers & Jokat, 2009). The northern part of the KR spreads more asymmetrically, with rates of 7.1 mm/y and 5.9 mm/y for the west and east blocks, respectively (Dumais et al., 2021). Opening of the north Atlantic initiated from the south to the north around 56 Ma (Crane et al., 1988; Talwani & Eldholm, 1977). The beginning of the spreading process at the MR is estimated to start in the Early Miocene (10–20 Ma; Engen et al., 2008). For the KR, the most recent interpretation puts the opening of the northern part of the KR at ca. 20 Ma with the possibility of a ridge jump at around 18 Ma (Dumais et al., 2021).

Glacial isostasy is another important component of the current state of stress in the Fram Strait. The entirety of Fennoscandia, the Barents Sea and Svalbard experienced an isostatic response to the glacial load up to 800 m in the last million years (Fjeldskaar & Amantov, 2018). The transition zone between the uplift and subsidence due to glacial isostasy may be responsible for high seismic activity offshore mid Norway and in the SW Barents Sea (Fjeldskaar et al., 2000; Olesen et al., 2013). The area to the east of the MR along the shelf edge was under the influence of glaciations at least for the past 3.6 Ma (Knies et al., 2009), with a local intensification of glacial-interglacial cycles occurring around 2.7 Ma (e.g., Faleide et al., 1996; Mattingsdal et al., 2014). Glacial stress modeling suggests that the area between the MR and the west-Svalbard margin shelf break is within the merged Greenland and Barents Sea forebulge zone (Vachon et al., 2022). The changes in the stress field over the glacial cycles have potentially influenced fault kinematics and fluid migration processes in the entire region.

Large amounts of sediments deposited within the west-Svalbard continental margin make gravitational loading a potential source of local stress field perturbations. In addition to varying extent of ice since the Late Pliocene, large amounts of hemipelagic sediments were deposited along the continental margin (e.g., Faleide et al., 1996). Strong deep-water currents drive the sediment transport and deposition in the form of contourites (Eiken & Hinz, 1993). Along the northern part of the KR valley, there is a 600 m height (seafloor depth) asymmetry between the eastern and western ridge flanks interpreted as the result of sediment loading in the eastern portion (Crane et al., 2001; Engen et al., 2003, 2008; Faleide et al., 1996; Kvarven et al., 2014), with at least 850–950 m of sediments deposited on this flank and within the valley (Amundsen et al., 2011; Kvarven et al., 2014). The thickest sequence of sediments formed the Vestnesa Ridge contourite drift to the NE from the MTF, with the estimated thickness of more than 5 km in places (Eiken & Hinz, 1993).

One way of constraining the current state of stress in the region is earthquake monitoring. The influence of the rift system on the current tectonic regime has been reported from seismological observations for decades in the area using land stations (e.g., Engen et al., 2003; Gibbons et al., 2017). Sparse station coverage and large distances (>100 km) from nearest land hamper the monitoring of both ridge system and intraplate seismicity, which in turn could inform about current tectonic processes affecting contourite deposits (e.g., the Vestnesa Ridge) and the fault structures outcropping north of the KR northward termination. For this reason, there is a large uncertainty in the location of earthquakes and their hypocentral depths, leading to an imprecise seismological image of the region (Figure 1; Bondár & Storchak, 2011). Temporary deployments of ocean bottom seismometers (OBS) allow the detection of lower magnitude earthquakes in targeted investigations along Arctic ridge boundaries (e.g., Jeddi et al., 2021; Meier et al., 2021; Schlindwein et al., 2015).

In this study we document the results of a long-term (11 months) OBS survey that targeted the area of bathymetric scarps characterized by thick sedimentary deposits over oceanic and continental crust off the north-west Svalbard coast. This area is wedged between the intersection of the KR and the MTF from the south and the Vestnesa Ridge contourite drift to the north and north-east. In this study, our aim was to investigate the present-day stress regime and the influence of oblique spreading on sedimentary faulting, fluid flow within the sedimentary cover and seafloor seepage. At the same time, the network placement allowed us to better constrain the spreading ridge system seismicity, particularly at the Molloy Transform Fault and the northern part of the Knipovich Ridge.

2. Deep Marine Fluid Flow Systems in the Fram Strait

One of the most investigated gas hydrate and seepage systems in the Arctic is that of the Vestnesa Ridge. Vestnesa Ridge is a contourite drift that continuously seeps methane through sedimentary faults and fractures at the crest of its eastern segment (e.g., Bünz et al., 2012; Panieri et al., 2017; Plaza-Faverola et al., 2015). The system was predominantly created from sediments deposited by the contourite currents driven by the deep-water exchange between Arctic and Atlantic oceans that started between 17 and 10 Ma ago (Ehlers & Jokat, 2009; Eiken & Hinz, 1993; Jakobsson et al., 2007). The N-S oriented pattern of current sediment deposition along the west-Svalbard shelf edge was influenced by the spreading direction of the oceanic seafloor leading to the NW turn of the ridge crest (Johnson et al., 2015: Figure 1). The youngest seismic facies consist of glaciomarine contourites with a component of turbidites close to the shelf edge, reflecting the onset of Pleistocene glaciations (Eiken & Hinz, 1993; Mattingsdal et al., 2014). To the southwest, major contourite drift deposits are characterized by scarps/faults visible on bathymetry data. These scarps extend from the northern termination of the ultra-slow spreading Knipovich Ridge toward north and north-west (Figure 1).

Along the NW-SE oriented portion of the Vestnesa Ridge crest, systems of pockmarks point to the past and present episodes of methane seepage (Bünz et al., 2012; Vogt & Crane, 1994). Gas hydrates with the underlying free gas accumulations are identified from seismic reflection data along the entire length of the Vestnesa Ridge (Goswami et al., 2015; Hustoft et al., 2009; Petersen et al., 2010; Plaza-Faverola et al., 2017; Singhroha et al., 2016, 2019). Presently documented seepage is contained within the eastern part of the ridge crest, but past seepage activity on the western segment of the system is well documented in sediments, seismic data, and bathymetry (Cooke et al., 2023; Consolaro et al., 2015; Plaza-Faverola et al., 2015; Vogt & Crane, 1994). Current seepage activity from pockmarks occurs at the termination of sub-seafloor fluid flow fault systems (Plaza-Faverola et al., 2015). The orientation of the faults (from 3D high-resolution seismic data) is similar to the bathymetric scarps propagating northward from the Knipovich Ridge; therefore, a potential link has been suggested (Plaza-Faverola et al., 2015). The creation of the bathymetric scarps itself was postulated to be an indication of the present-day northward propagation of the spreading Knipovich Ridge (Crane et al., 2001).

The presence of gas hydrate deposits and free gas accumulations have also been documented for almost the entire area with the bathymetric scarps between the Vestnesa Ridge and KR using seismic interpretation (Madrussani et al., 2010; Vanneste et al., 2005). Tidally modulated seafloor gas emissions have been inferred from pressure and temperature data about 20 km to the east-southeast from the area presented in this study (Sultan et al., 2020). Active seafloor seepage observed on hydroacoustic measurements was recently documented at one of the seafloor pockmarks adjacent to sedimentary faults north of the KR (Plaza-Faverola, 2022).

The process behind the spatial variation in the currently observed seepage is still a matter of debate. In the past (<160 ka), seepage intensification episodes at the Vestnesa Ridge have been directly linked to the time shortly after glacial maxima, placing the highest emphasis on glacially induced stress as a factor driving fault activation and seepage activity (Himmler et al., 2019; Schneider et al., 2018). Seepage activity here has also been proposed to be associated with an extensional stress regime generated from the northward propagation of the KR (e.g., Plaza-Faverola & Keiding, 2019; Vanneste et al., 2005). At present day, the extensional forcing from ridge spreading, glacial isostatic adjustment, and gravitational stress due to the sediment loading are all considered as potential culprits controlling deep marine seepage activity in the region (Plaza-Faverola et al., 2015; Plaza-Faverola & Keiding, 2019; Vachon et al., 2022).

3. Data and Methods

3.1. OBS Network Deployment and Recovery

The data we used for this study is a part of an experiment intended to constrain the stress regime and its role on fault-controlled seepage in the west-Svalbard margin. A network of closely spaced OBSs (10 instruments separated within 10 km from its closest neighbor) was intended to record any potential earthquake associated with sedimentary faults to the north of the KR termination (Figure 1). The aim was to infer the dominant tectonic stress regime locally, based on focal mechanisms from recorded earthquakes.

The instruments were dropped freely to the seafloor in August 2020 and recovered in July 2021 during cruises CAGE20-5 (Bünz, 2023) and CAGE21-3 (Plaza-Faverola, Schlindwein, et al., 2022) onboard R/V Helmer Hanssen. Each station was located approximately 10 km apart from all of its nearest neighbors. All stations except VSN02 and VSN10 were equipped with a Trillium Compact broadband seismometer (sensitive down to periods of 120 s). These OBSs were provided by the German Instrument Pool for Amphibian Seismology DEPAS (Schmidt-Aursch & Haberland, 2017). Stations VSN02 and VSN10 used instrumentation from UiT—The Arctic University of Norway. These consisted of short-period geophones with 4.5 Hz corner frequency commonly used for active source high resolution experiments (e.g., Singhroha et al., 2020). Additionally, each unit had a hydrophone attached to its frame. Each OBS recorded data continuously with a sampling frequency of 100 Hz.

3.2. Preprocessing

3.2.1. Relocation

We established the true position of each OBS on the seafloor (red triangles in Figure 1) using active seismic surveys conducted directly after the deployment. We used the direct arrival of the P wave from hundreds of seismic shots with known positions and inverted the travel-time equation for the OBS location with the smallest

root-mean-square (RMS) error. For the calculations, we assumed an average P wave velocity in the water column of 1,500 m/s. We estimated the average error in positioning stations to be smaller than 10 m.

3.2.2. Time Correction of Data

We synchronized the internal clock of each OBS recording unit with the GPS signal prior to deployment and after recovery, and thus established the absolute clock drift (skew) for all stations except VSN03, VSN04, VSN06, and VSN09 (Table S1 in Supporting Information S1). For these stations, a synchronization of the clocks after recovery was not possible. Prior experience with the clocks of the recording units showed that the assumption of a linear drift of the clock is not always valid. We followed the cross-correlation procedure described by Hannemann et al. (2014) to independently determine the time-dependent clock drift for each station. We filtered the data in the frequency range of 0.1–1 Hz and correlated the recorded signal daily between station pairs using a window of 250 s length with 50% overlap (a subset of the plots is presented in Figures S1 and S2 in Supporting Information S1). Based on the results, we assumed that station VSN01 had a linear drift and the absolute skew value for it was known from the clock synchronization after recovery (Table S1 in Supporting Information S1). Therefore, we selected it as a reference station and applied a linear skew correction to it. We then repeated cross-correlations between VSN01 and all other stations to determine the time-dependent clock drift for other instruments (Figures S3–S11 in Supporting Information S1). We found that only for stations VSN04 and VSN06 (in addition to VSN01), a linear skew correction would be correct. We subsequently fitted a third-degree polynomial to all established skew curves and applied daily, linear corrections approximating the fitted curve for each station. In the final step, we verified the correct skew adjustment by a final round of pair-wise cross-correlations (Figures S12 and S13 in Supporting Information S1). We found the residual skew being lower than the expected accuracy of the manual picking of seismic phases of about 0.2 s, thus acceptable for further data analysis (Figure S14 in Supporting Information S1).

3.3. Earthquakes Recorded by the OBS Network

3.3.1. Detection and Phase Picking

We conducted a search for earthquakes at each station using the short-term average/long-term average (STA/LTA) picker (Allen, 1982), and we subsequently identified actual earthquake detections using a Random Forest classifier on time windows around each potential event (Hibert et al., 2014, 2017; Provost et al., 2017). We adjusted the parameters of the STA/LTA detector to the expected local seismicity in the area in the following fashion: STA window length–0.8 s, LTA window length–45 s, detection start ratio–7 and detection end ratio–1.5. For the event classification, we used a model trained previously on events recorded by a different experiment at the Vestnesa Ridge (Domel et al., 2023). We manually verified all detections recognized as earthquakes and found 358 events with a signal-to-noise ratio high enough to manually pick seismic phases for at least one station. We subsequently picked P and S wave arrival times (where possible) for all stations using the SEISAN software package (Havskov & Ottemöller, 1999; Havskov et al., 2020). The pick uncertainty is about 0.2 s.

3.3.2. Earthquake Location Procedure

Initial locations showed that seismicity is present mostly outside of the seismic network, which makes the estimation of a minimum 1D velocity model difficult using common procedures such as VELEST (Kissling et al., 1995). We therefore used the following forward approach, applying the HYPOSAT location algorithm for estimating earthquake locations (Schweitzer, 2001). Instead of inverting seismic velocities from our earthquake records, we used seismic velocity constraints from a nearby seismic refraction study (Ritzmann et al., 2004). Seismic velocities within the shallow sediments (up to 1,600 m below the seafloor) were obtained from P-wave reflection tomography available in the study area (Madrussani et al., 2010). In the initial testing, we tried different Vp/Vs ratios and chose 1.69 for the final model evaluation. We represented the shallow sediments as two layers with fixed layer boundary depths at 350 and 1,600 m below the seafloor. For the upper layer, we tested Vp velocities between 1.5–1.9 km/s for Vp (Figure 2). Similarly, for the bottom layer, we tested velocities between 1.8–2.1 km/s. The section of the model below 1,600 m depth was derived from the refraction study (Ritzmann et al., 2004), and remained mostly fixed in the analysis. We tried different depths of the crust-mantle boundary to better match the parts of the refraction profile closest to our study area and varied slightly the P-wave velocity in the upper mantle (between 7.9–8.1 km/s). All individual variations of velocity resulted in 18 different models tested model (Figure 2).

10.1029/2023GC011174

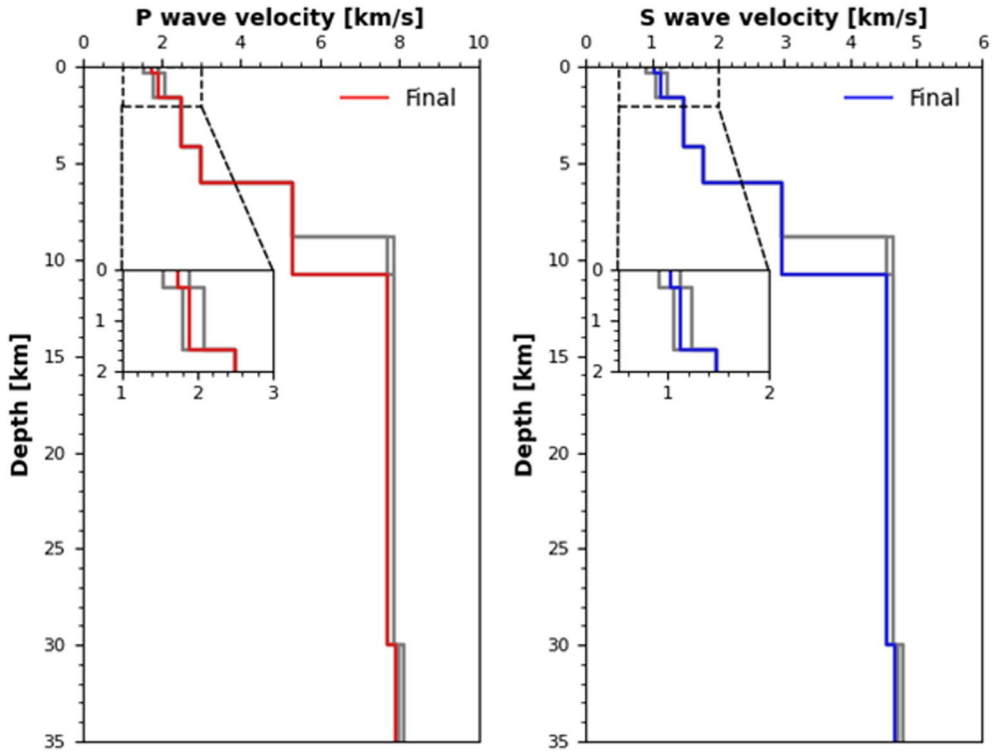

Figure 2. An overview of all velocity models tested for relocation in the HYPOSAT software. Color lines represent the final models used to obtain earthquake locations for P and S waves, red and blue, respectively.

To compare the effect of the different velocity functions on event relocation, we first located all events using a regional velocity model (BAREY; Hicks et al., 2004) with a fixed hypocenter depth of 10 km and selected a small subset of earthquakes meeting the following criteria: RMS error <0.8 s, number of used seismic phases >20, average error ellipse size <10 km, and maximum distance from the center of the network <50 km.

The resulting subset of 46 earthquakes was repeatedly located with all 18 different versions of our local velocity model for fixed hypocenter depths of 8,10,12,15,25, and 30 km, respectively. To obtain a location solution for each pair of model variant and fixed hypocenter depth, three iterations with HYPOSAT were performed, using the average station residual of all earthquakes as a station correction term in the subsequent iteration. It is important to keep in mind that we cannot reliably establish depths of earthquakes located further than twice the focal depth from the station and without dense azimuthal coverage (e.g., Havskov et al., 2011), which in our case means outside the deployed network. For thin oceanic crust in spreading zones, earthquakes usually originate at depths of about 0–30 km (e.g., Schlindwein & Schmid, 2016). The fixed earthquake depths used in relocation were selected to minimize errors in the positioning of the events but cannot be interpreted in a meaningful way. Consequently, we refrained from discussing the hypocentral depth of earthquakes.

For each event, we selected the fixed-depth location with the lowest RMS error and lowest average error ellipse size as the final solution for the respective velocity model variant. We then computed average values of the RMS error and the error ellipse size for all events within each velocity model variant. In this way, we could compare the performance of the different velocity models. We selected the model that had both the lowest average RMS error and average error ellipse (red line in Figure 2). In the testing, we found that the differences between different models were ultimately very small and obtained earthquake locations very similar (max. 0.01 s for the average RMS error, less than 0.2 km for the average error ellipse). The final 1D velocity model was used by HYPOSAT up to an epicentral distance of 1° (approx. 111 km) from each station. Events at larger distances were located using the regional velocity model BAREY (Hicks et al., 2004).

We subsequently located all 358 earthquakes using the final velocity model and for each event we retained the result with the fixed depth that produced the smallest RMS error. For further analysis, we only used events that

met the following criteria: RMS error <0.4 s, minimum number of stations with seismic phases used ≥3 and average error ellipse <10 km. The resulting dataset contained 254 earthquakes. We include the plots of residual times for P and S phase picks (the difference between computed and observed travel times of waves) in the supplement (Figures S15 and S16 in Supporting Information S1).

3.3.3. Local Magnitude Estimation

We calculated local magnitudes based on manual picks of the maximum amplitude of the S wave train on the horizontal channels of the Wood-Anderson simulated OBS data (e.g., Hutton & Boore, 1987; Kanamori & Jennings, 1978). We used the formula of Hutton and Boore with the default parameters (Hutton & Boore, 1987). Using the maximum curvature method (Wiemer & Wyss, 2000; Wyss et al., 1999), we estimated a magnitude of completeness Mc of 2.5 for our earthquake dataset.

3.4. Other Earthquake Catalogs

For the general overview of the regional seismicity in the past decades, we used the International Seismological Center (ISC) Reviewed Bulletin that compiles phase picks from all seismological networks in the area and provides its own hypocenter solutions (Bondár & Storchak, 2011). We plotted all events in the area from 1980–2020 that had an RMS error <3 s, contributed phases of at least 10 stations to the location solution, and had magnitudes ≥2.0 (Figure 1). These selection criteria resulted in 580 earthquakes.

We further searched for earthquakes that occurred during our experiment and were detected both on land and by our network. For that purpose, we referred to the bulletin of the Norwegian National Seismic Network (NNSN) (Ottemöller et al., 2018). In addition to the stations on Svalbard and in Norway, it routinely incorporates the phase picks from the Danish seismological stations in Greenland. We used all locations with the RMS error ≤2 s for our analysis, resulting in a total of 293 earthquakes.

Out of 358 earthquakes detected and located by the OBS network, we identified 170 that were also recorded on land and included in the NNSN bulletin. For these events, we additionally obtained the phase picks of the land stations. We manually matched each individual event between the catalogs and combined the phase picks from land stations and OBS stations to relocate the events using HYPOSAT. Our goal was to determine the best constrained location for each earthquake and therefore we compared the locations results and errors from using the OBS network only, the NNSN reported locations, and finally, a relocation combining the phase picks of both networks. For the relocation with combined phase picks, we repeated the same procedure as when using only OBS observations. Locating earthquakes using phase picks from stations in vastly different geological conditions with large differences in crustal thickness to be accommodated in a 1D velocity model led to overall higher location errors. We therefore considered earthquakes as well located when an RMS error <1 s (compared to 0.4 s when using OBS data only). With this criterion, we retained 85 of the 170 earthquakes as well located for further analysis.

4. Results

4.1. Regional Seismicity

Our OBS network detected and reliably located the regional seismicity in an area comprising of the nearby oceanic ridges: the Molloy Ridge (MR), the northernmost part of the Knipovich Ridge (KR), the Molloy Transform Fault (MTF) and the coast of Svalbard (Figure 3). Almost all seismicity is concentrated along the North American and the Eurasian plate boundaries and is related to the plate motion. Events at the MR seem to occur well within the bathymetric outline of the ridge axis. Along the MTF, earthquakes are closely aligned with the fault outline in the north-western part and positioned slightly to the southwest in the south-eastern part of the fault (Figure 3). We notice a large number of earthquakes originating from the KR but spread out in the easterly direction. Based on bathymetry data, there is an obvious clustering of events at the outside corner, away from what seems to be the rift valley of the KR. This area is bounded toward the north by a fault, the prolongation of the MTF that extends past the KR rift valley toward Svalbard (Figure 3). Hereafter, we refer to this area as the outside corner between the MTF and the KR–OC area (Figure 3). We did not observe seismicity propagating northwards from the KR and no earthquakes were detected within the deployed network during the survey. We detected 2 weak earthquakes of magnitudes 1.2 and 2.0, respectively, close to the crest of the Vestnesa Ridge to the north from the OBS network

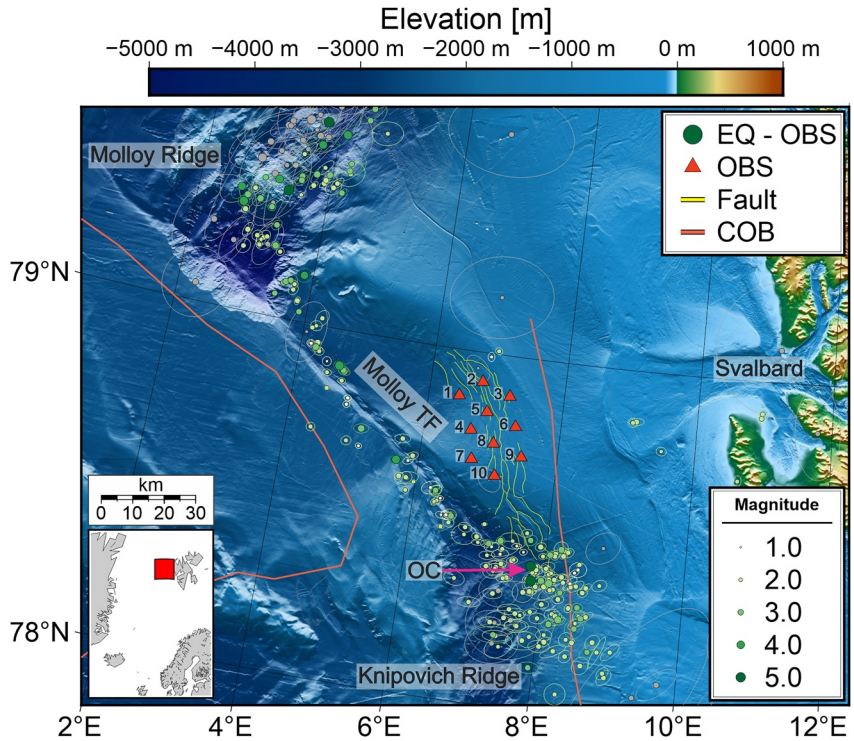

Figure 3. Regional map of the seismicity with all earthquake locations obtained during the ocean bottom seismometer (OBS) deployment (August 2020–July 2021). Circles around each location represent the error ellipse for each earthquake. Colors correspond to the magnitude, as shown in the legend. Earthquakes and circles in gray are locations below the accuracy criteria selected (RMS error <0.4 s, minimum number of stations with seismic phases used ≥3 and average error ellipse <10 km). OC marks the location of the outside corner of the Knipovich Ridge—Molloy Transform Fault intersection discussed more in the text. The rest of the labels and bathymetry are the same as in Figure 1.

(Figure 3; waveforms in Figures S18–S21 in Supporting Information S1). Additional three weak ($M < 3$) events occurred close to the shelf edge on the west coast of Svalbard and a few similarly small earthquakes are visible near to and at the mainland of the archipelago.

Throughout the duration of the survey, earthquakes occurred in all the described areas without any larger temporal clusters of seismicity, such as earthquake swarms or prominent main shock—after shock sequences, apart from a few sporadic small clusters in the rift valleys. The magnitudes of the well-located events from Figure 3 are between 0.9 and 5.3. Among the strongest $M > 4$ events, most are contained within the rift valley of the MR. Two out of four events with magnitudes $M > 5$ originate there as well, but the other two are observed in the outside corner between the MTF and KR (Figure 3).

4.2. Quality Assessment of the Obtained Seismicity Map

We do not observe earthquakes occurring within the network during the survey; hence, we focus on the analysis of the recorded earthquake epicenter distribution. The residual times of P and S phase picks used in earthquake location show good reliability of the results (Figures S15 and S16 in Supporting Information S1). The majority of the picks are distributed narrowly around zero, with a symmetric distribution indicating correct phase identification. The P phase picks are mostly contained in a range between −0.2 and 0.2 s for all the stations (between −0.4 and 0.4 s for S phase picks). The largest deviation from the symmetric pattern and above ranges of residuals is for stations VSN02 and VSN10, and because of the generally larger residuals, these are also the stations utilized the least in the relocation process. The elongation of our network in NW-SE direction (Figures 1 and 3) leads to a preferred orientation of the semi-major axis of the error ellipses in SW-NE direction for the earthquakes in the northern part of the KR. Therefore, it is especially important to critically assess the accuracy of earthquake locations from the MTF and the outside corner between the MTF and KR before suggesting any geological interpretation for the area. We accomplish this by comparison of OBS-derived earthquake locations to well constrained

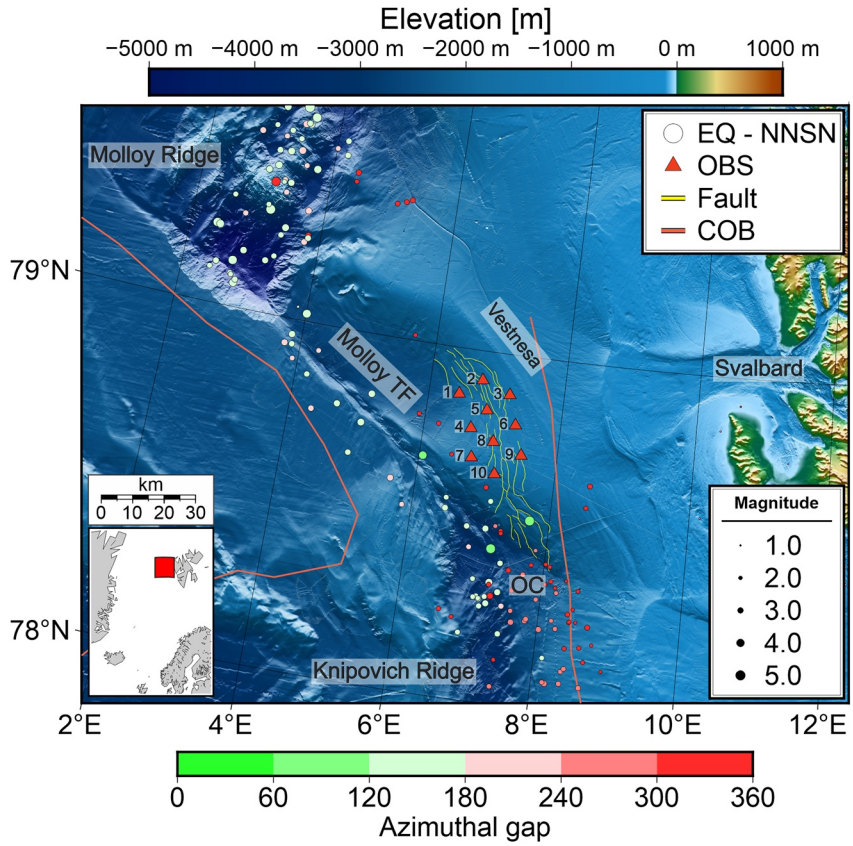

Figure 4. Earthquakes recorded and located in the study area by Norwegian National Seismic Network (NNSN) using observations from permanent land stations. The color of the circle represents the azimuthal gap of seismic phase observations. All other information and data used are the same as Figures 1 and 3.

ISC results since 1960, one-to-one comparisons of the earthquake locations obtained using OBS data and NNSN bulletin, and relocations of the observed events using combined phase picks from the OBS network and provided by the NNSN bulletin.

4.2.1. Comparison With the ISC Reviewed Bulletin

The observed seismicity in the ISC Reviewed Bulletin in the last 40 years appears to be much more spread out along the plate boundaries, especially along the MTF (Figure 1). Most of the earthquakes are located southwest of the bathymetric expression of the fault outline. Some events are also reported in the area of the fault scarps on the Vestnesa Ridge flanks within our OBS network. Seismicity in the vicinity of the MR is dispersed in the eastern direction, with many events located in the western part of the Vestnesa Ridge sedimentary drift. The presence of seismicity in the outside corner between the MTF and KR (OC in Figure 1) is clearly visible here, in the same manner as in our study (Figure 3). Events with magnitudes ≥5 are located within the bathymetric outline of this feature. Likewise, a similar shift of the earthquake locations eastward in the northern part of the KR can be observed. Overall, we see that the seismicity pattern recorded by our OBS network is in a good agreement with the longer-term observations provided by the ISC Bulletin, but our network yields a sharper image of the seismicity with less scatter and more focused earthquake locations along the plate boundaries.

4.2.2. Comparison With the Regional NNSN Bulletin for the Duration of the OBS Survey

The results of the observations by the NNSN regional network during the time period of the OBS deployment do not differ drastically from the seismicity map obtained from the OBS data (Figure 4). We plot the NNSN earthquake locations color-coded by the azimuthal gap of observations, which can help determine which events are observed from many different directions and for which the observations are limited mostly to seismic stations on Svalbard. We see that well-recorded events with a low azimuthal gap are located in close vicinity of the

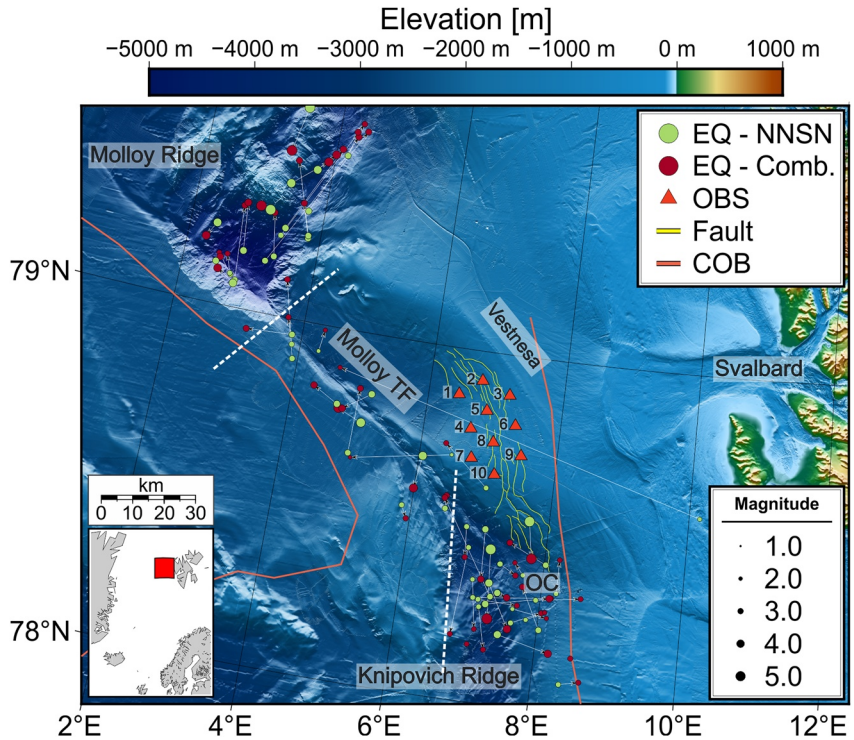

Figure 5. Regional map of seismicity showing the difference between observations from Norwegian National Seismic Network (NNSN; green circles) and earthquake locations when phase picks from OBS data are included (Combined; red circles), with arrows showing the change in each individual event position. Other labels and symbols are the same as in Figures 1, 3, and 4).

plate boundaries. Earthquakes along the MTF are more spread out compared to our OBS data, and again a large portion of them is situated to the southwest of the fault outline. As in our survey, there is seismicity present at the outside corner between the MTF and KR intersection (OC in Figure 4); however, most observations by the NNSN have limited azimuthal coverage, lacking phase arrivals west of the KR, mainly from Greenland. Since some of the events there have a magnitude as high as 4.0, we suspect that the ridge prevents wave propagation toward the west. Two strong ($M \geq 5.0$) events, which are located by our OBS network close to each other in the outside corner between the MTF and KR, have locations in the KR ridge valley and north of the corner, toward the fault scarps of the Vestnesa Ridge (outlined in yellow in Figure 4). NNSN locates two earthquakes close to the shelf edge, southeast of our OBS network. These events are visible in the OBS data, but the noise levels are too high to make accurate phase picks. In general, we can say that the despite the confined nature of our OBS network, the recorded seismicity seems to be better aligned with the dominant tectonic structures of the region than the earthquakes located in the same time period by the NNSN regional network.

Table 1
Median Epicenter Shift of Earthquake Locations and Circular Mean of Epicenter Shift Azimuth Between the Observations of NNSN Network (Land Data) and Locations for the Same Events When Phase Picks From OBS Data Are Included (Combined Observations)

Region	Median epicenter shift [km]	Circular mean of epicenter shift azimuth [°]	Circular standard deviation of epicenter shift [°]
Molloy Ridge	12.7	332	74
Molloy Transform Fault	12.2	346	66
Knipovich Ridge	13.1	89	91

Note. Earthquakes are split into three separate groups, roughly encompassing the Molloy Deep, the Molloy Transform Fault and the Knipovich Ridge (separation shown on Figure 5). Angle of 0° correspond to the geographic North, with the clockwise direction of increasing angles.

4.2.3. Joint Observations of Seismicity With the OBS Data and NNSN Phase Picks

Merging the phase observations from the NNSN network with our marine data leads to a large rearrangement of originally NNSN-reported locations (Figure 5). We split the seismicity map into three regions, approximately separating the KR, MTF, and MR to compute the average epicenter shift and median azimuth of it (Table 1; dashed lines in Figure 5). Weak events with small azimuthal coverage experience the largest shift and become positioned closer to the plate boundaries and their newly determined locations are very close to the results from OBS data only (Figure 3). The median amount of the distance that epicenters shifted is very similar for all regions (Table 1). Across the MR, there is a noticeable trend of moving hypocenters toward the

NW and NE directions (circular mean of epicenter shift azimuth of 332; Table 1); however, the new locations are still following the bathymetric outline of the rift valley. The seismicity along the MTF exhibits a similar shift of epicenter distance and the circular mean of epicenter shift azimuth is similar to the MR (Table 1). The overall image of seismicity does not change there between the maps, with the exception of an event reported close to the mainland being relocated to the MTF and a number of events being moved either from southwards of the fault outline northwards or vice versa. Overall, the locations obtained from combining the datasets are more closely aligned along the MTF than the positions reported in NNSN bulletin and do not greatly differ from the locations obtained from OBS data. At the outside corner between the MTF and KR and on the northern part of the KR itself, the events are generally moved eastward when seismic phases from OBS data are included (circular mean of epicenter shift azimuth of 89 in Table 1). Some events exhibit a large shift southward, including one earthquake of a magnitude $M > 5.0$ that is now positioned much further south and not anymore on the extension of the MTF propagating southeast. Inversely, a second similarly large event that was located north of the outside corner between the MTF and KR is now placed directly on the large fault outline and its location is almost identical to the position obtained from only the OBS data (Figures 3 and 5). Inversely, it can be said that combining phase picks from OBS and NNSN catalog generally shifts the epicenter westward compared to seismicity map from only OBS data (Figure S17 in Supporting Information S1). Combining the phase observations from OBS and NNSN data leads to smaller azimuthal gaps for earthquakes, particularly in the KR area, but the overall RMS errors of the resulting locations are higher (0.46 vs. 0.16 s, compared to the locations of these events from OBS data). Therefore, at least for the earthquakes close to the OBS network, the obtained locations using the combined datasets are likely less accurate. Ultimately, in all of the discussed catalogs the occurrence of seismicity in the outside corner between the MTF and KR is clearly visible.

4.2.4. Rationale for an Interpretable Local Seismicity Catalog

Since all of the earthquakes located by our OBS stations are outside the designed network, it is important to determine for how big of an area the obtained local seismicity catalog provides more accurate results compared to regional and global bulletins and can be interpreted with regards to the local geology. The general seismicity pattern is similar to decadal observations provided by the ISC, but with a better alignment to the plate boundaries. We focus on two important observations in the later sections. First is the presence of seismicity in the outside corner between the MTF and KR, visible as a spread-out cloud of earthquakes on ISC data (OC in Figure 1). Observations from the nearby OBS network confirm this and with the relocation combining OBS phases with NNSN land observations we verify that events with a low azimuthal coverage in the NNSN catalog, while rearranged, are still present in this corner (Figures 3–5). In this process, we also position an $M > 5.0$ earthquake directly on the bathymetric outline of the MTF extension in a location almost identical to the one obtained from just OBS data (Figures 3 and 5). Second, there is a visible shift of earthquake locations to the southwest of the MTF outline. It is seen as more earthquakes located there in all of the catalogs discussed (Figures 3–5). Overall, the observed pattern does not change by much when we combine land and marine observations.

We put a conservative limit of 50 km from the geographic midpoint of the OBS network as an area for which we interpret the earthquake catalog (Figure 6). This value is based on the average RMS error of the calculated hypocenters and the larger number of weak events observed compared to those reported in the land NNSN catalog (Figures 3 and 4). The magnitude $M > 5.0$ earthquake in the outside corner between the MTF and KR within this limit has an RMS error of 1.7 s in the NNSN catalog and 0.4 s when adding OBS phases and relocating. For the same event, location from OBS data has the RMS error decreased to 0.22 s. For all of the events reported in the NNSN catalog and seen on OBS data within this radius, locations from OBS data show a decrease in the average RMS error from 1.05 to 0.17 s. For the given radius, the NNSN catalog provides only 15 earthquake locations compared to a total of 68 observed on OBS data during the same time period. Therefore, at least for events located at the MTF and northern portion of the KR, we believe that the OBS-based hypocenter locations are more reliable and the overall image of seismicity is more detailed. The resulting catalog includes in addition two earthquakes on the Vestnesa Ridge sedimentary drift and two events on the shelf edge, none of which were reported on land (Figure 6).

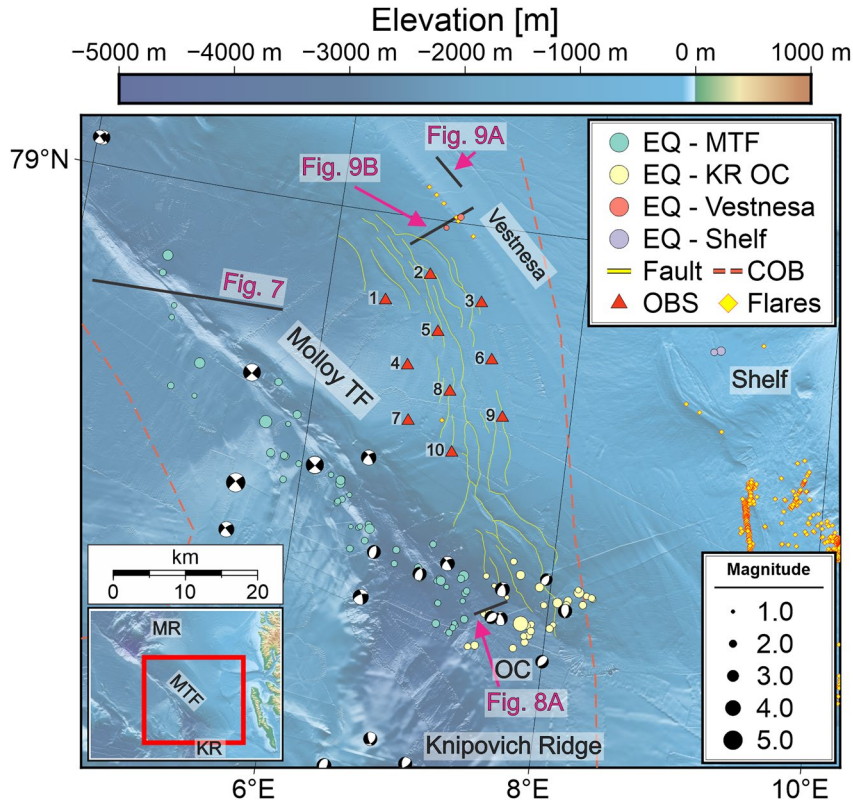

Figure 6. A close-up map of the area in the vicinity of the OBS network, with the earthquake locations computed using only OBS data. Earthquakes are differentiated by colors into groups that are individually discussed in the text. In addition, all available earthquakes with focal mechanisms between 1980 and 2020 provided by the International Seismological Center (ISC) are plotted. Pink lines show the locations of seismic profiles discussed in the text, with the corresponding figure number. Yellow squares with the red outline indicate all currently documented seepage sites in the area (e.g., Panieri et al., 2017; Smith et al., 2014). Other labels are the same as in Figures 1, 3–5.

5. Discussion

5.1. Tectonic Activity at the Plate Boundary

Our observations, in agreement to land seismological bulletins, show continuous energy release (stress drop) along the transform boundary at the MTF. The obtained dataset of seismic locations shows earthquake activity outside of the bathymetric outline of the MTF (blue events in Figure 6). This activity is observed on decadal observations of ISC and 2020–2021 observations from NNSN but for these observations could be interpreted as a hypocenter uncertainty due to limitations of the 1D velocity modeling and/or a relative distance between the earthquakes and recording stations. We suggest that the shift of the earthquakes in the southeastern part of the MTF is a real phenomenon and the majority of earthquake energy release occurs at or to the southwest of the MTF outline (at the North American Plate). In the OBS dataset, this shift is larger than the calculated hypocenter uncertainty for these events. The pattern of earthquake distribution is consistent with the presence of a highly and recently faulted sedimentary cover south of the MTF and a largely undisturbed sedimentary cover north of it (Figure 7). Recent sedimentary faulting appears to be a consequence of seismically active crustal faults. The presence of sedimentary faults connected to larger crustal structures is documented for the southern side from the bathymetric outline and additional seismic data further northwest along the MTF (Waghorn et al., 2020).

The bathymetric scarps north of the Knipovich Ridge termination were previously interpreted as a sign of northwards propagation of the KR (Crane, et al., 2001), following the previous early Cenozoic structures of Spitsbergen Shear Zone (Crane et al., 1991), and this rationale was assumed in several further studies in the area (Hustoft et al., 2009; Plaza-Faverola et al., 2015; Vanneste et al., 2005). This interpretation was based only on bathymetric data, and so far, no deep-reaching faults with a potential connection to the crust have been observed on the seismic lines in the area of bathymetric scarps (Dumke et al., 2016). Past seismic studies for this location imaged only

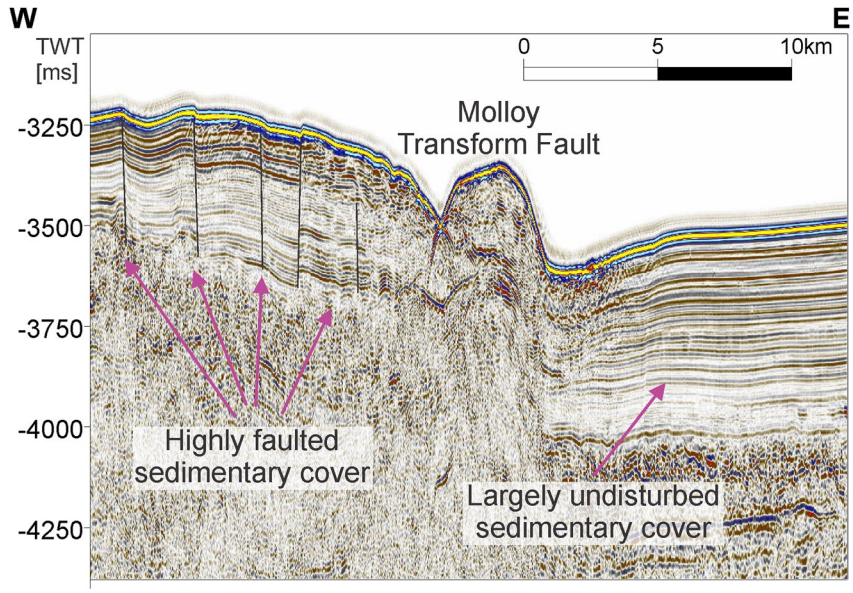

Figure 7. Seismic profile crossing the Molloy Transform Fault (location marked in Figure 6).

the youngest sediments up to 0.78 Ma (Vanneste et al., 2005). During our OBS deployment, we have not detected signs of seismicity at these fault scarps or beneath them, with the exception of the flanks in the vicinity of the outside corner between the MTF and KR (Figure 6). With the network specifically designed to monitor seismicity within the scarps area, we were unable to record any earthquakes within the network, thus we conclude that the sedimentary faults do not accommodate seismically any large tectonic movement (i.e., at least often enough to be recorded during the survey). In this area, the estimated thickness of the sediments is about 4–5 km (Ritzmann et al., 2004). Our results support inferences from a refraction study by Ritzmann et al. (2004), where the basement subsidence due to the heavy sedimentary load may explain the evolution of outcropping gravitational faults. Their presence may also be the result of the gravitational forcing at the steep edges of the sedimentary drift (Plaza-Faverola & Keiding, 2019) deposited steadily through the deep-water currents along the margin boundary since the post Late Miocene (Eiken & Hinz, 1993; Hustoft et al., 2009).

Within the interpretable seismicity map, we see a number of earthquakes originating eastward from the northernmost part of the KR, beyond the rift valley into the outside corner between the MTF and KR, and partially in the location of southernmost bathymetric scarps targeted by the survey (Figure 6). Generally, fracture zones outside the ridge-transform fault intersection have been classically considered inactive, however several zones worldwide have major earthquake activity in these zones documented (Bohnenstiehl et al., 2004; Lay, 2019). The observed activity in the OC area is frequent, and with at least one earthquake of $M > 5$, comparable in energy to the strongest earthquakes recorded in the region. It is also visible in both the ISC catalog between 1980 and 2020 as well as in NNSN catalog during the duration of our survey. The OC area is characterized by gently sloping seafloor toward the KR rift valley. A recent interpretation of aeromagnetic data indicates the rift jump at 18 Ma in this section of the KR eastward, with the failed rift segment identified more than 100 km to the west at the present day (Dumais et al., 2021). The valley itself in this part is estimated to be covered by up to 950 m of sediments (Amundsen et al., 2011) and is currently spreading at a rate of 7.1 mm/y and 5.9 mm/y for the west and east section, respectively (Dumais et al., 2021). The total thickness of the sediments at the eastern flank of the KR ridge valley is around 850–950 m here (Kvarven et al., 2014), with the thickness at the corner likely greater due to shallower water depth (therefore larger sediment thickness measured from the crust). The sediments in the flank were previously determined to be predominantly glacial-hemipelagic deposits sourced from the western-Svalbard margin (Amundsen et al., 2011; Kvarven et al., 2014) and not older than the Late Pliocene—Pleistocene age (Amundsen et al., 2011). The rapid sedimentation from the eastern direction, modulated by glacial and inter-glacial periods since Late Pliocene (Knies et al., 2009), led to greater amount of sediments deposited on the eastern flank compared to the western one at the northern portion of the KR due to sediment load (Crane et al., 2001; Engen et al., 2003, 2008; Faleide et al., 1996; Kvarven et al., 2014). This

10.1029/2023GC011174

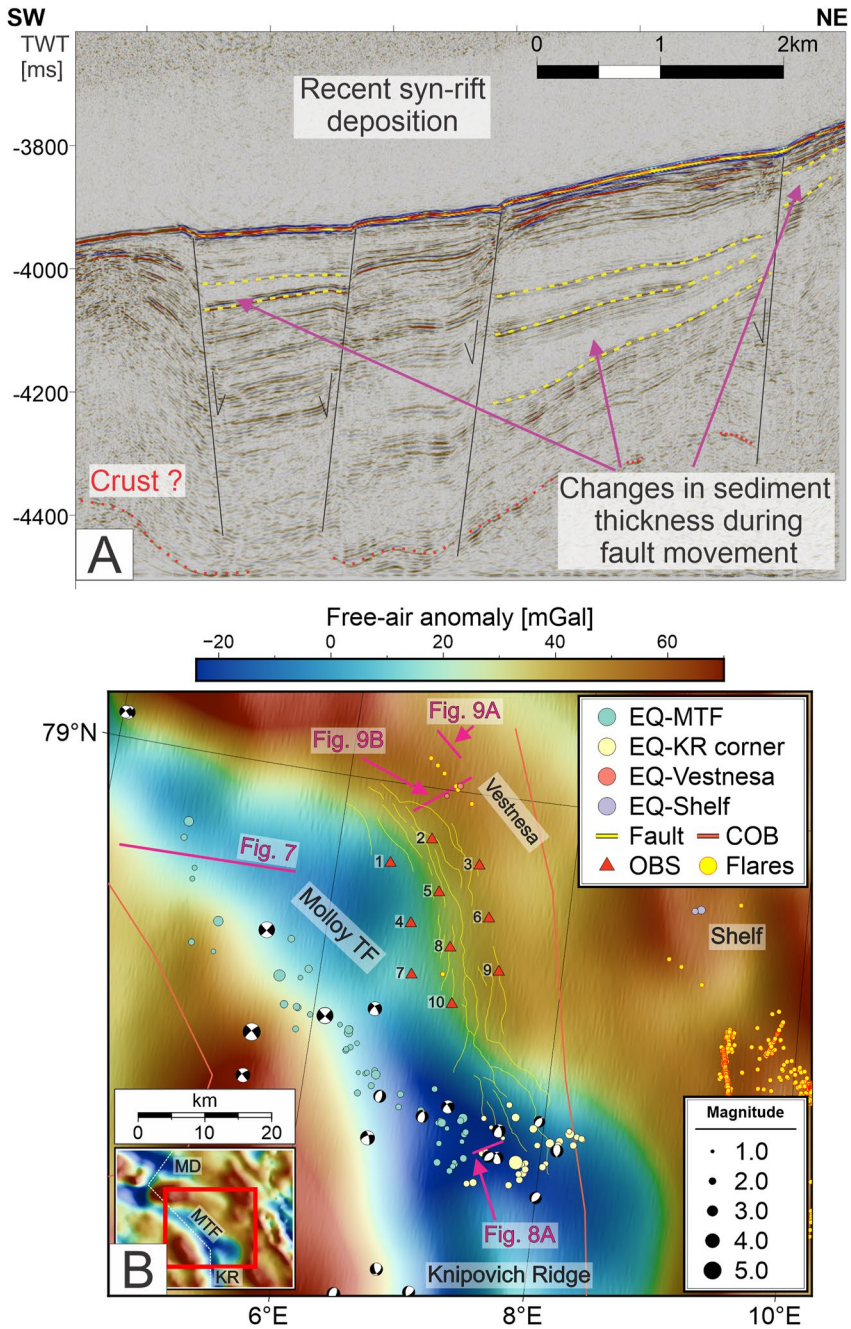

Figure 8. (a) Seismic profile located at the outside corner between the Molloy Transform Fault and the Knipovich Ridge (location in Figure 6). Several young normal faults show difference in the layers' thicknesses, indicating syn-rift deposition (b) Free-air gravity anomaly map of the same area as in Figure 6 (Sandwell et al., 2014), showing a negative gravity anomaly extending eastwards from the Knipovich Ridge bathymetric outline. All other features labeled in the same way as in Figure 6.

corresponds to water depths greater in the west part by about 600 m on average (Kvarven et al., 2014). A section of the seismic line recorded over the outside corner between the MTF and KR shows a clear indication of recent syn-rift deposition (i.e., increase in the thickness of sedimentary layers toward active fault planes) over a potential crustal ridge structure (Figure 8a). Therefore, we propose that the outside corner between the KR and MTF represents a sediment-filled continuation of the rift valley and the inactive fracture zone is located further eastward. The ridge valley is generally oriented in the north-east direction along the entire length of the KR, following the documented orientation of magmatic centers' axial high trends (Crane et al., 2001). This interpretation is

supported by the available focal mechanism solutions provided by the ISC bulletin (Bondár & Storchak, 2011), showing a gradual change from the strike-slip pattern along the MTF all the way to normal faulting in the outside corner (Figures 6 and 8b). Additionally, a strong low-gravity free-air anomaly is visible in this corner (Figure 8b), which can correspond either to the spreading center as seen along the MR, MTF and along the KR to the south, but also reflect the sedimentary infill (Dumais et al., 2022; gravity data from Sandwell et al., 2014). The earthquake activity ceases roughly at the newly revised continental-oceanic margin boundary (Dumais, et al., 2022; COB line in Figures 6 and 8b) and is most likely limited to the oceanic portion of the crust.

5.2. Seismicity Along the Vestnesa Ridge Sedimentary Drift

During the 11-month survey, we recorded only two earthquakes close to the Vestnesa Ridge sedimentary drift crest (Figures 6 and 8b; waveforms and phase picks in Figures S18–S21 in Supporting Information S1). These have local magnitudes of 1.2 and 2.0; therefore, we assume that the detection sensitivity was about $M = 1.0$ for this area. High resolution seismic data across and along the ridge crest show evidence of normal faulting through the Quaternary sedimentary cover (Figure 9). Two major sedimentary fault planes are oriented parallel or nearly parallel to the MR spreading axis (Figure 9a). In the direction perpendicular to the ridge crest, we see the top of the ridge with a documented near-surface fluid flow system and the gas accumulations related to seepage, but also one of the bathymetric scarps on the south-western flank of the ridge that we interpret as a gravitational fault (Figure 9b). No spatial changes in layer thickness indicate recent faulting, markedly different from the example from the outside corner between the MTF and the KR (Figure 7). Based on the fault geometry, the age constraint of one of the reflections at 2.7 Ma (Mattingsdal et al., 2014; Plaza-Faverola et al., 2015), and the opening time of the MR dated currently at 10–20 Ma (Engen et al., 2008), we consider the direct influence of present-day drift at the MR on the generation of these two normal faults unlikely (Figure 9a). However, it is possible that the orientation of these faults (parallel or near parallel to the MR spreading axis) is a result of the dominant orientation of stresses in the shallow subsurface established during the seafloor spreading (namely that underlying crustal faults may be accommodating stress generated by the sedimentary weight). It is unlikely that the present-day tectonic faulting at the MTF would influence the fault generation in both seismic profiles due to the lack of observed seismicity northwards from its bathymetric outline in the OBS data (Figure 6) and the general paucity of earthquakes reported for this part of the region (Figure 1).

Vestnesa Ridge lies close to the inferred continental-oceanic crust boundary. However, most recent (Dumais et al., 2021 COB line in Figures 6 and 8b), and previous estimations (Engen et al., 2008) locate the earthquakes at the crest of the Vestnesa at least 15 km from the boundary, reducing the probability of any potential interactions between the oceanic and continental crust as a factor in earthquake generation.

In the past 3.6 Ma, the shelf area to the east of the Vestnesa Ridge was under the cyclic influence of propagating and retreating ice masses (Knies et al., 2009). The changes in the regional stress regime due to glacial processes in the past can be a factor influencing current tectonic processes, with the potential for even large magnitude earthquakes (e.g., Steffen et al., 2021; Thorson, 2000). Recent modeling of the lithospheric response to the past glaciation cycles suggests that the glacial processes contribute to the current day stress regime and can influence existing fault structures, but the degree of this influence has to be further quantified (Vachon et al., 2022). Therefore, post glacial subsidence along the continental slope and rise may be a factor contributing to the generation of earthquakes at the Vestnesa Ridge and near the shelf break (purple events in Figures 6 and 8).

5.3. Implications of Neotectonics for Fault-Controlled Fluid Seepage in the Fram Strait

We observe that two of the earthquakes from the Vestnesa Ridge are in a vicinity of the ridge portion that is currently seeping methane from the seafloor (yellow squares in Figures 6 and 8b, e.g., Panieri et al., 2017; Smith et al., 2014). Plausible determination of the mechanism responsible for the two observed events is therefore especially important in the context of the current and past gas seepage that has been reported and studied there (e.g., Bünz et al., 2012; Hustoft et al., 2009; Panieri et al., 2017; Plaza-Faverola et al., 2015). There is a strong evidence for modulations of gas seepage during the recent glacial and interglacial periods in the seismic data (Plaza-Faverola et al., 2015). The dating of sedimentary cores points to a correlation between the glacial cycles and increased seepage directly after the glacial maxima; therefore, several authors proposed glacial tectonics as the dominant force behind the seepage activity cycles (Himmler et al., 2019; Schneider et al., 2018). These

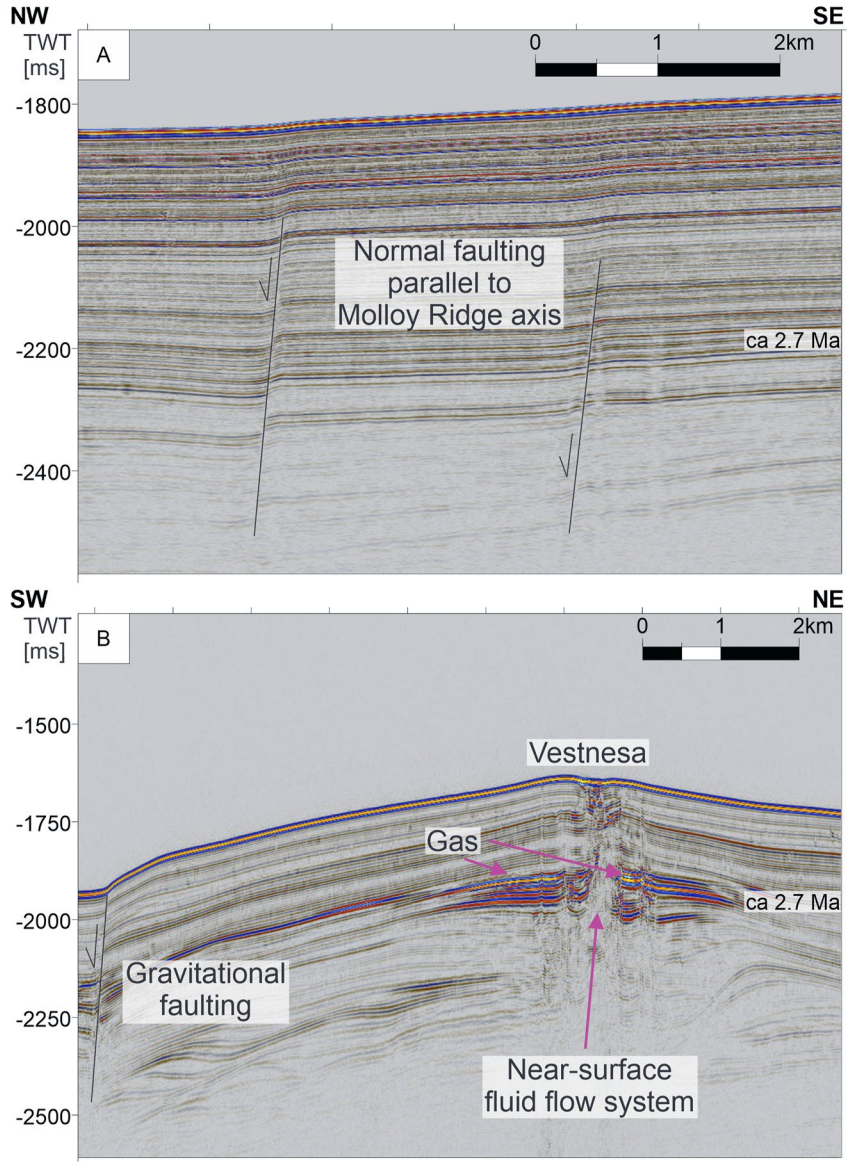

Figure 9. Two high resolution seismic profiles in the area of the Vestnesa Ridge contourite drift: one parallel to the ridge crest (a), and one perpendicular, crossing the well-studied fluid flow system (b). Faults in the profile (a) are parallel or near parallel to the orientation of the ultraslow spreading Molloy Ridge. In the profile (b), one of the bathymetric features investigated with the OBS dataset (yellow lines in e.g., Figure 6) is interpreted as a gravitational fault.

observations cannot however explain why a similar group of seafloor structures (pockmarks), further west on the crest of the ridge, connected to the recent (>8,000 years ago) seepage activity, is presently dormant (Consolaro et al., 2015; Cooke et al., 2023; Plaza-Faverola et al., 2015). It was previously suggested that the spatial variation in seepage activity is driven predominantly by the tectonic forces from the seafloor spreading at the MR and KR (Plaza-Faverola & Keiding, 2019; Plaza-Faverola et al., 2015). Our observations of seismicity at the Vestnesa Ridge (or lack of thereof) imply little or no rifting influence at present time. The orientation of normal faults visible in the profile parallel to the Vestnesa (Figure 9a) can however point to a reactivation of deeper crustal faults established in the normal fault spreading regime under the sediment weight. The connection to the deeper structures cannot be however resolved using the high-resolution seismic data available for this study. Nevertheless, it is perhaps not surprising that the only two earthquakes recorded near the VR crest using the OBS array discussed here are located proximal to the most prominent seepage activity along the sedimentary ridge (Figures 6 and 8b).

Moreover, recent seepage activity documented southward (Figures 6 and 8b) is also adjacent to a seismologically active zone (i.e., the MTF/KR outside corner; Figures 6 and 8b).

Two observed earthquakes occurred close to the ridge crest, where the overall sediment thickness is greatest and the flanks of the crest are steepest (e.g., Eiken & Hinz, 1993). We do not observe seismic activity where sediment thickness is lower and/or their deposition is close to horizontal, in the area between the Vestnesa Ridge and MTF, but also to the north (Figure 3). Therefore, we propose that the sediment loading driven by the depositional pattern is playing an important role in the seepage distribution in the area. The stress orientation and the main fault structures in the crust for this area should under normal circumstances be established near the spreading centers in the past and remain extensional while the crust progressively is moved toward the continental margin. It is possible that the observed seismicity and reported seepage activity are related to the reactivation of deeper tectonic structures oriented parallel to the spreading MR by the gravitational weight of the sediments and the process can be selectively dependent on the direction of older faults and the shape of deposited sedimentary structures (e.g., Bellahsen & Daniel, 2005; Brandes et al., 2011; Dubois et al., 2002). This reactivation can be influenced by isostatic rebalancing after the glaciations (e.g., Redfield et al., 2005; Steffen et al., 2014; Vachon et al., 2022), Alternatively, it is entirely possible that the difference in the glacial stress field between now and the last glacial maximum (23 ka) is significant enough to reactivate faults and influence seepage activity in the region (Vachon et al., 2022). These observations support what has been inferred in previous studies, namely that sedimentary faults to the north of the KR termination are prone to dilation and favor fluid migration and seepage (Plaza-Faverola et al., 2015; Vachon et al., 2022).

While we do not observe present day seismicity and therefore a direct link between the ridge system and the fluid flow system at the Vestnesa, the rift structures indirectly control sedimentary faulting. Since the initial opening of the Fram Strait, the systems of current circulation developed along the newly forming KR rift valley and started depositing sediments on the young ocean floor (e.g., Amundsen et al., 2011; Eiken & Hinz, 1993; Engen et al., 2008). The intensification of Northern Hemisphere glaciation and the resulting influx of hemipelagic deposits, together with the differential motion of plates between the MTF, caused offshore extension of the sediment deposition and the westward facing progression of the Vestnesa Ridge crest (Johnson et al., 2015). This means that the plate motion between the MTF was partially responsible for the shift in the sediment deposition direction from roughly north-south to the east-west visible today, therefore influencing the gravitational faulting direction along the flanks of the created sedimentary rift. This change in the faulting orientation can be followed looking at the bathymetric outline of the faults along the structure (yellow lines in Figures 6 and 8a), and the current day W-E orientation can be seen in the seismic data perpendicular to the ridge crest (Figure 9b). Therefore, even if the faulting, and by extension, the seepage currently occurring at the Vestnesa Ridge are not controlled by the present-day ocean spreading, the direction of fault planes and the location of observed, sparse seismicity may be the aftermath of the sediment drift depositional history, strongly influenced by the very same plate motion.

6. Conclusions

We investigated the local stress regime at the oblique spreading ridge setting of the eastern Fram Strait using seismological observations. We used the data from an ocean bottom seismometer (OBS) network with 10 instruments that was recorded over 11 months between August 2020 and July 2021. We studied earthquakes to understand the regional distribution of present-day tectonic processes and their connection to shallow fault systems, for some of which seafloor gas seepage has been previously documented. This temporary OBS survey between the northern termination of the Knipovich Ridge and the Vestnesa Ridge contourite drift led to the following observations and potential explanations for the spatial patterns of seismicity observed:

- Along the MTF, most of the seismicity is located at or to the south-southwest in relation to the bathymetric outline of the fault zone. This observation is supported by the long-term observations of the seismicity in the region and seismic data indicating recent faulting of sediments to the south-southwest from the MTF and undisturbed shallow sediments in the north-northeastern direction.
- The outside corner between the MTF and KR, seen as an extension of the MTF eastwards from the KR ridge valley, is an active tectonic area with the reported normal-faulting and frequent, large magnitude earthquakes. We propose that this region represents a sediment-covered northernmost portion of the active spreading zone,

indicated by the syn-rift deposition of recent sedimentary deposits and the observed frequent seismic activity in the OBS data, but also in long-term studies.

- We do not observe any local earthquakes within the bathymetric faults ("scarps") to the north of the northward termination of the KR and the earthquake activity seems to be constrained to the vicinity of the KR termination. Therefore, we suggest that structures visible on the seafloor are likely gravitational faults created due to the sediment load and gravitational sliding, possibly influenced by the glacial subsidence modeled for the area at present. There seems to be no connection between the faults and northward propagation of the KR, as suggested in the past.
- The observations at the MTF and the outside corner between the MTF and KR indicate a potential connection between deeper crustal faults (as evidenced by earthquakes) and shallow sediments (as indicated by near-surface fault structures in seismic data). We observe two weak (M 1.2 & 2.0) earthquakes close to the Vestnesa Ridge crest that are likely caused by processes similar to ones responsible for bathymetric scarps further south. High-resolution seismic data indicate that some of the buried sedimentary faults perpendicular to the Vestnesa Ridge crest have comparable orientation to the rift structures at the Molloy Ridge. Observed earthquakes may suggest crustal fault reactivation, and stress accommodation in the form of extensional sedimentary faults that promote gas leakage. The direct link to deeper structures cannot be established without seismic data with greater penetration depth. The sparse seismic activity without a direct connection to the MR, MTF and KR makes a propagation of present-day spreading from the plate boundaries into the sedimentary deposits on the Eurasian plate unlikely.

Conflict of Interest

The authors declare no conflicts of interest relevant to this study.

Data Availability Statement

The raw dataset is archived at PANGAEA (Plaza-Faverola, Domel, et al., 2022; https://doi.pangaea.de/10.1594/PANGAEA.952424) and available in GEOFON repository under the network code Y9 (https://geofon.gfz-potsdam.de/). The data is under embargo until 31.12.2024. The input files for location software (HYPOSAT), including phase picks for all processed events and the final earthquake location results are freely available at UiT The Arctic University of Norway's data repository DataverseNO (Domel, 2023; https://doi.org/10.18710/TP4CMS). The land data earthquake catalog was obtained from the International Seismological Centre (ISC) Seismological Dataset Repository (https://doi.org/10.31905/6TJZECEY) and Norwegian National Seismic Network (NNSN; Ottemöller et al., 2018). The ObsPy package was used for processing of the seismological data (Krischer et al., 2015; www.obspy.org). All maps were created using Generic Mapping Tools - GMT (Wessel et al., 2019). Bathymetry of the region provided by the International Bathymetric Chart of the Arctic Ocean (IBCAO) (Jakobsson et al., 2020). Free-air gravity anomaly map provided by Sandwell et al. (2014). An estimate of continental-oceanic transition boundary obtained from Norwegian Geological Institute (Dumais et al., 2021).

Acknowledgments
This work is conducted as a part of the SEAMSTRESS project, supported by the Tromsø Research Foundation (TFS) and the Research Council of Norway (Grant 287865). The work was also supported by the Research Council of Norway through its Centers of Excellence funding scheme Grant 223259 (Centre for Arctic Gas Hydrate, Environment and Climate—CAGE). We thank the crew of R/V Helmer Hanssen, Mechita Schmidt-Aursch and Henning Kirk for their support during deployment and recovery of OBSs. We additionally thank Mechita Schmidt-Aursch for the help with processing and data management of the OBS dataset. We are grateful for the machine learning classification codes provided by Clément Hibert. We also thank Marie-Andrée Dumais for sharing the outline of the revised continent-ocean margin boundary for plotting.

References

Allen, P. A., & Allen, J. R. (2013). *Basin analysis: Principles and application to petroleum play assessment*. John Wiley & Sons.

Allen, R. (1982). Automatic phase pickers: Their present use and future prospects. *Bulletin of the Seismological Society of America*, *72*(6B), S225–S242. https://doi.org/10.1785/bssa07206b0225

Amundsen, I. M. H., Blinova, M., Hjelstuen, B. O., Mjelde, R., & Haflidason, H. (2011). The Cenozoic western Svalbard margin: Sediment geometry and sedimentary processes in an area of ultraslow oceanic spreading. *Marine Geophysical Researches*, *32*(4), 441–453. https://doi.org/10.1007/s11001-011-9127-z

Bellahsen, N., & Daniel, J. M. (2005). Fault reactivation control on normal fault growth: An experimental study. *Journal of Structural Geology*, *27*(4), 769–780. https://doi.org/10.1016/j.jsg.2004.12.003

Bohnenstiehl, D. R., Tolstoy, M., & Chapp, E. (2004). Breaking into the plate: A 7.6 Mw fracture-zone earthquake adjacent to the Central Indian Ridge. *Geophysical Research Letters*, *31*(2), L02615. https://doi.org/10.1029/2003gl018981

Bondár, I., & Storchak, D. (2011). Improved location procedures at the international seismological Centre. *Geophysical Journal International*, *186*(3), 1220–1244. https://doi.org/10.1111/j.1365-246x.2011.05107.x

Brandes, C., Polom, U., & Winsemann, J. (2011). Reactivation of basement faults: Interplay of ice-sheet advance, glacial lake formation and sediment loading. *Basin Research*, *23*(1), 53–64. https://doi.org/10.1111/j.1365-2117.2010.00468.x

Bünz, S. (2023). CAGE20-5 cruise report: Tectonic stress studies and seismic surveys on the West-Svalbard margin. *CAGE – Centre for Arctic Gas Hydrate, Environment and Climate Report Series*, *8*. https://doi.org/10.7557/cage.6914

Bünz, S., Polyanov, S., Vadakkepuliyambatta, S., Consolaro, C., & Mienert, J. (2012). Active gas venting through hydrate-bearing sediments on the Vestnesa Ridge, offshore W-Svalbard. *Marine Geology*, *332*, 189–197. https://doi.org/10.1016/j.margeo.2012.09.012

Carter, L., Gavey, R., Talling, P. J., & Liu, J. T. (2014). Insights into submarine Geohazards from breaks in Subsea telecommunication cables. *Oceanography*, *27*(2), 58–67. https://doi.org/10.5670/oceanog.2014.40

Consolaro, C., Rasmussen, T. L., Panieri, G., Mienert, J., Bunz, S., & Sztybor, K. (2015). Carbon isotope (delta C-13) excursions suggest times of major methane release during the last 14 kyr in Fram Strait, the deep-water gateway to the Arctic. *Climate of the Past*, *11*(4), 669–685. https://doi.org/10.5194/cp-11-669-2015

Cooke, F., Plaza-Faverola, A., Bünz, S., Sultan, N., Ramachandran, H., Bedle, H., et al. (2023). Sedimentary deformation relating to episodic seepage in the last 1.2 million years: A multi-scale seismic study from the Vestnesa Ridge, eastern Fram Strait. *Frontiers in Earth Science*, *11*. https://doi.org/10.3389/feart.2023.1188737

Crane, K., Doss, H., Vogt, P., Sundvor, E., Cherkashov, G., Poroshina, I., & Joseph, D. (2001). The role of the Spitsbergen shear zone in determining morphology, segmentation and evolution of the Knipovich Ridge. *Marine Geophysical Researches*, *22*(3), 153–205. https://doi.org/10.1023/a:1012288309435

Crane, K., Sundvor, E., Buck, R., & Martinez, F. (1991). Rifting in the northern Norwegian-Greenland Sea: Thermal tests of asymmetric spreading. *Journal of Geophysical Research*, *96*(B9), 14529–14550. https://doi.org/10.1029/91jb01231

Crane, K., Sundvor, E., Foucher, J. P., Hobart, M., Myhre, A. M., & LeDouaran, S. (1988). Thermal evolution of the western Svalbard margin. *Marine Geophysical Researches*, *9*(2), 165–194. https://doi.org/10.1007/bf00369247

Dick, H. J. B., Lin, J., & Schouten, H. (2003). An ultraslow-spreading class of ocean ridge. *Nature*, *426*(6965), 405–412. https://doi.org/10.1038/nature02128

Domel, P. (2023). Replication data for: "Local seismicity and sediment deformation in the west Svalbard margin: Implications of neotectonics for seafloor seepage" [Dataset]. DataverseNO. https://doi.org/10.18710/TP4CMS

Domel, P., Hibert, C., Schlindwein, V., & Plaza-Faverola, A. (2023). Event recognition in marine seismological data using Random Forest machine learning classifier. *Geophysical Journal International*, *235*(1), 589–609. https://doi.org/10.1093/gji/ggad244

Dubois, A., Odonne, F., Massonnat, G., Lebourg, T., & Fabre, R. (2002). Analogue modelling of fault reactivation: Tectonic inversion and oblique remobilisation of grabens. *Journal of Structural Geology*, *24*(11), 1741–1752. https://doi.org/10.1016/s0191-8141(01)00129-8

Dumais, M. A., Gernigon, L., Olesen, O., Johansen, S. E., & Brönner, M. (2021). New interpretation of the spreading evolution of the Knipovich Ridge derived from aeromagnetic data. *Geophysical Journal International*, *224*(2), 1422–1428. https://doi.org/10.1093/gji/ggaa527

Dumais, M. A., Gernigon, L., Olesen, O., Lim, A., Johansen, S. E., & Brönner, M. (2022). Crustal and thermal heterogeneities across the Fram Strait and the Svalbard margin. *Tectonics*, *41*(10). https://doi.org/10.1029/2022tc007302

Dumke, I., Burwicz, E. B., Berndt, C., Klaeschen, D., Feseker, T., Geissler, W. H., & Sarkar, S. (2016). Gas hydrate distribution and hydrocarbon maturation north of the Knipovich Ridge, western Svalbard margin. *Journal of Geophysical Research: Solid Earth*, *121*(3), 1405–1424. https://doi.org/10.1002/2015jb012083

Ehlers, B.-M., & Jokat, W. (2009). Subsidence and crustal roughness of ultra-slow spreading ridges in the northern North Atlantic and the Arctic Ocean. *Geophysical Journal International*, *177*(2), 451–462. https://doi.org/10.1111/j.1365-246x.2009.04078.x

Eiken, O., & Hinz, K. (1993). Contourites in the Fram Strait. *Sedimentary Geology*, *82*(1–4), 15–32. https://doi.org/10.1016/0037-0738(93)90110-q

Engen, Ø., Eldholm, O., & Bungum, H. (2003). The Arctic plate boundary. *Journal of Geophysical Research*, *108*(B2). https://doi.org/10.1029/2002jb001809

Engen, Ø., Faleide, J. I., & Dyreng, T. K. (2008). Opening of the Fram Strait gateway: A review of plate tectonic constraints. *Tectonophysics*, *450*(1–4), 51–69. https://doi.org/10.1016/j.tecto.2008.01.002

England, W. A., Mackenzie, A. S., Mann, D. M., & Quigley, T. M. (1987). The movement and entrapment of petroleum fluids in the subsurface. *Journal of the Geological Society*, *144*(2), 327–347. https://doi.org/10.1144/gsjgs.144.2.0327

Etiope, G. (2015). *Natural gas seepage: The Earth's hydrocarbon degassing*. Springer.

Faleide, J. I., Solheim, A., Fiedler, A., Hjelstuen, B. O., Andersen, E. S., & Vanneste, K. (1996). Late Cenozoic evolution of the western Barents Sea-Svalbard continental margin. *Global and Planetary Change*, *12*(1–4), 53–74. https://doi.org/10.1016/0921-8181(95)00012-7

Fjeldskaar, W., & Amantov, A. (2018). Effects of glaciations on sedimentary basins. *Journal of Geodynamics*, *118*, 66–81. https://doi.org/10.1016/j.jog.2017.10.005

Fjeldskaar, W., Lindholm, C., Dehls, J. F., & Fjeldskaar, I. (2000). Postglacial uplift, neotectonics and seismicity in Fennoscandia. *Quaternary Science Reviews*, *19*(14), 1413–1422. https://doi.org/10.1016/s0277-3791(00)00070-6

Gardner, J. V., van den Ameele, E. J., Gelfenbaum, G., Barnhardt, W., Lee, H., & Palmer, S. (2001). Mapping southern Puget Sound delta fronts after 2001 earthquake. *Eos, Transactions American Geophysical Union*, *82*(42), 485–489. https://doi.org/10.1029/01eo00287

Gibbons, S. J., Harris, D. B., Dahl-Jensen, T., Kværna, T., Larsen, T. B., Paulsen, B., & Voss, P. H. (2017). Locating seismicity on the Arctic plate boundary using multiple-event techniques and empirical signal processing. *Geophysical Journal International*, *211*(3), 1613–1627. https://doi.org/10.1093/gji/ggx398

Goswami, B. K., Weitemeyer, K. A., Minshull, T. A., Sinha, M. C., Westbrook, G. K., Chabert, A., et al. (2015). A joint electromagnetic and seismic study of an active pockmark within the hydrate stability field at the Vestnesa Ridge, west Svalbard margin. *Journal of Geophysical Research: Solid Earth*, *120*(10), 6797–6822. https://doi.org/10.1002/2015jb012344

Hannemann, K., Krüger, F., & Dahm, T. (2014). Measuring of clock drift rates and static time offsets of ocean bottom stations by means of ambient noise. *Geophysical Journal International*, *196*(2), 1034–1042. https://doi.org/10.1093/gji/ggt434

Havskov, J., Bormann, P., & Schweitzer, J. (2011). Seismic source location. In P. Bormann (Ed.), *New manual of seismological observatory practice 2 (NMSOP-2), Potsdam: Deutsches GeoForschungszentrum GFZ* (pp. 1–36).

Havskov, J., & Ottemöller, L. (1999). SEISAN earthquake analysis software. *Seismological Research Letters*, *70*(5), 532–534. https://doi.org/10.1785/gssrl.70.5.532

Havskov, J., Voss, P. H., & Ottemöller, L. (2020). Seismological observatory software: 30 Yr of SEISAN. *Seismological Research Letters*, *91*(3), 1846–1852. https://doi.org/10.1785/0220190313

Hibert, C., Mangeney, A., Grandjean, G., Baillard, C., Rivet, D., Shapiro, N. M., et al. (2014). Automated identification, location, and volume estimation of rockfalls at Piton de la Fournaise volcano. *Journal of Geophysical Research: Earth Surface*, *119*(5), 1082–1105. https://doi.org/10.1002/2013jf002970

Hibert, C., Provost, F., Malet, J.-P., Maggi, A., Stumpf, A., & Ferrazzini, V. (2017). Automatic identification of rockfalls and volcano-tectonic earthquakes at the Piton de la Fournaise volcano using a Random Forest algorithm. *Journal of Volcanology and Geothermal Research*, *340*, 130–142. https://doi.org/10.1016/j.jvolgeores.2017.04.015

Hicks, E. C., Kvaerna, T., Mykkeltveit, S., Schweitzer, J., & Ringdal, F. (2004). Travel-times and attenuation relations for regional phases in the Barents Sea Region. *Pure and Applied Geophysics*, *161*(1), 1–19. https://doi.org/10.1007/s00024-003-2437-6

Himmler, T., Sahy, D., Martma, T., Bohrmann, G., Plaza-Faverola, A., Bünz, S., et al. (2019). A 160,000-year-old history of tectonically controlled methane seepage in the Arctic. *Science Advances*, *5*(8), eaaw1450. https://doi.org/10.1126/sciadv.aaw1450

Hudec, M. R., & Jackson, M. P. A. (2004). Regional restoration across the Kwanza Basin, Angola: Salt tectonics triggered by repeated uplift of a metastable passive margin. *AAPG Bulletin*, *88*(7), 971–990. https://doi.org/10.1306/02050403061

Hustoft, S., Bunz, S., Mienert, J., & Chand, S. (2009). Gas hydrate reservoir and active methane-venting province in sediments on < 20 Ma young oceanic crust in the Fram Strait, offshore NW-Svalbard. *Earth and Planetary Science Letters*, *284*(1–2), 12–24. https://doi.org/10.1016/j.epsl.2009.03.038

Hutton, L. K., & Boore, D. M. (1987). The ML scale in southern California. *Bulletin of the Seismological Society of America*, *77*(6), 2074–2094. https://doi.org/10.1785/bssa0770062074

Jakobsson, M., Backman, J., Rudels, B., Nycander, J., Frank, M., Mayer, L., et al. (2007). The early Miocene onset of a ventilated circulation regime in the Arctic Ocean. *Nature*, *447*(7147), 986–990. https://doi.org/10.1038/nature05924

Jakobsson, M., Mayer, L. A., Bringensparr, C., Castro, C. F., Mohammad, R., Johnson, P., et al. (2020). The international bathymetric chart of the Arctic Ocean version 4.0. *Scientific Data*, *7*(1), 176. https://doi.org/10.1038/s41597-020-0520-9

Jeddi, Z., Ottemöller, L., Sørensen, M. B., Rezaei, S., Gibbons, S. J., Strømme, M. L., et al. (2021). Improved seismic monitoring with OBS deployment in the Arctic: A pilot study from offshore western Svalbard. *Seismological Research Letters*, *92*(5), 2705–2717. https://doi.org/10.1785/0220200471

Johnson, J. E., Mienert, J., Plaza-Faverola, A., Vadakkepuliyambatta, S., Knies, J., Bünz, S., et al. (2015). Abiotic methane from ultraslow-spreading ridges can charge Arctic gas hydrates. *Geology*, *43*(5), 371–374. https://doi.org/10.1130/g36440.1

Judd, A., & Hovland, M. (2007). *Seabed fluid flow: The impact on geology, biology, and the marine environment*. Cambridge University Press.

Kanamori, H., & Jennings, P. C. (1978). Determination of local magnitude, ML, from strong-motion accelerograms. *Bulletin of the Seismological Society of America*, *68*(2), 471–485.

Kissling, E., Kradolfer, U., & Maurer, H. (1995). *Program VELEST user's guide-short introduction*. Institute of Geophysics.

Knies, J., Matthiessen, J., Vogt, C., Laberg, J. S., Hjelstuen, B. O., Smelror, M., et al. (2009). The Plio-Pleistocene glaciation of the Barents Sea–Svalbard region: A new model based on revised chronostratigraphy. *Quaternary Science Reviews*, *28*(9–10), 812–829. https://doi.org/10.1016/j.quascirev.2008.12.002

Krischer, L., Megies, T., Barsch, R., Beyreuther, M., Lecocq, T., Caudron, C., & Wassermann, J. (2015). ObsPy: A bridge for seismology into the scientific Python ecosystem. *Computational Science & Discovery*, *8*(1), 014003. https://doi.org/10.1088/1749-4699/8/1/014003

Kvarven, T., Hjelstuen, B. O., & Mjelde, R. (2014). Tectonic and sedimentary processes along the ultraslow Knipovich spreading ridge. *Marine Geophysical Researches*, *35*(2), 89–103. https://doi.org/10.1007/s11001-014-9212-1

Lay, T. (2019). Reactivation of oceanic fracture zones in large intraplate earthquakes? In *Transform plate boundaries and fracture zones* (pp. 89–104).

Madrussani, G., Rossi, G., & Camerlenghi, A. (2010). Gas hydrates, free gas distribution and fault pattern on the west Svalbard continental margin. *Geophysical Journal International*, *180*(2), 666–684. https://doi.org/10.1111/j.1365-246x.2009.04425.x

Mattingsdal, R., Knies, J., Andreassen, K., Fabian, K., Husum, K., Grøsfjeld, K., & De Schepper, S. (2014). A new 6 Myr stratigraphic framework for the Atlantic–Arctic Gateway. *Quaternary Science Reviews*, *92*, 170–178. https://doi.org/10.1016/j.quascirev.2013.08.022

Meier, M., Schlindwein, V., Scholz, J. R., Geils, J., Schmidt-Aursch, M. C., Kruger, F., et al. (2021). Segment-scale seismicity of the ultraslow spreading Knipovich ridge. *Geochemistry, Geophysics, Geosystems*, *22*(2), e2020GC009375. https://doi.org/10.1029/2020gc009375

Miall, A. D. (2013). *Principles of sedimentary basin analysis*. Springer Science & Business Media.

Olesen, O., Bungum, H., Dehls, J., Lindholm, C., Pascal, C., & Roberts, D. (2013). Neotectonics, seismicity and contemporary stress field in Norway–mechanisms and implications. *Quaternary Geology of Norway*, *13*, 145–174.

Ottemöller, L., Strømme, M., & Storheim, B. (2018). Seismic monitoring and data processing at the Norwegian national seismic network. *Summary of the Bulletin of the International Seismological Centre*, *52*(I), 27–40. https://doi.org/10.31905/1m97csyl

Panieri, G., Bunz, S., Fornari, D. J., Escartin, J., Serov, P., Jansson, P., et al. (2017). An integrated view of the methane system in the pockmarks at Vestnesa Ridge, 79 degrees N. *Marine Geology*, *390*, 282–300. https://doi.org/10.1016/j.margeo.2017.06.006

Paton, D. (2011). Post-rift deformation of the North East and south Atlantic margins: Are "passive margins" really passive? In *Tectonics of sedimentary basins* (pp. 249–269).

Petersen, C. J., Bünz, S., Hustoft, S., Mienert, J., & Klaeschen, D. (2010). High-resolution P-Cable 3D seismic imaging of gas chimney structures in gas hydrated sediments of an Arctic sediment drift. *Marine and Petroleum Geology*, *27*(9), 1981–1994. https://doi.org/10.1016/j.marpetgeo.2010.06.006

Plaza-Faverola, A. (2022). CAGE21-5 Cruise Report: Test of offshore instrumentation for in-situ sediment pressure measurements, west-Svalbard continental margin. *CAGE – Centre for Arctic Gas Hydrate, Environment and Climate Report Series*, *9*. https://doi.org/10.7557/cage.6721

Plaza-Faverola, A., Bünz, S., Johnson, J. E., Chand, S., Knies, J., Mienert, J., & Franek, P. (2015). Role of tectonic stress in seepage evolution along the gas hydrate-charged Vestnesa Ridge, Fram Strait. *Geophysical Research Letters*, *42*(3), 733–742. https://doi.org/10.1002/2014gl062474

Plaza-Faverola, A., Domel, P., Bünz, S., Schmidt-Aursch, M., & Schlindwein, V. (2022). Project SEAMSTRESS: DEPAS ocean-bottom seismometer operations on Vestnesa Ridge in 2020-2021 [Dataset]. PANGAEA. https://doi.org/10.1594/PANGAEA.952424

Plaza-Faverola, A., & Keiding, M. (2019). Correlation between tectonic stress regimes and methane seepage on the western Svalbard margin. *Solid Earth*, *10*(1), 79–94. https://doi.org/10.5194/se-10-79-2019

Plaza-Faverola, A., Schlindwein, V., Domel, P., Schmidt-Aursch, M., Cooke, F. A., Holm, T., & Jensen, S. A. (2022). CAGE21-3 cruise report: Ocean bottom seismics and acoustic surveys on the westwest-Svalbard margin—A study of local seismicity and its effect on methane seepage. *CAGE – Centre for Arctic Gas Hydrate, Environment and Climate Report Series*, *9*. https://doi.org/10.7557/cage.6722

Plaza-Faverola, A., Vadakkepuliyambatta, S., Hong, W. L., Mienert, J., Bunz, S., Chand, S., & Greinert, J. (2017). Bottom-simulating reflector dynamics at Arctic thermogenic gas provinces: An example from Vestnesa Ridge, offshore west Svalbard. *Journal of Geophysical Research-Solid Earth*, *122*(6), 4089–4105. https://doi.org/10.1002/2016jb013761

Provost, F., Hibert, C., & Malet, J. P. (2017). Automatic classification of endogenous landslide seismicity using the Random Forest supervised classifier. *Geophysical Research Letters*, *44*(1), 113–120. https://doi.org/10.1002/2016gl070709

Redfield, T. F., Osmundsen, P. T., & Hendriks, B. W. H. (2005). The role of fault reactivation and growth in the uplift of western Fennoscandia. *Journal of the Geological Society*, *162*(6), 1013–1030. https://doi.org/10.1144/0016-764904-149

Ritzmann, O., Jokat, W., Czuba, W., Guterch, A., Mjelde, R., & Nishimura, Y. (2004). A deep seismic transect from Hovgård Ridge to northwestern Svalbard across the continental-ocean transition: A sheared margin study. *Geophysical Journal International*, *157*(2), 683–702. https://doi.org/10.1111/j.1365-246x.2004.02204.x

Sandwell, D. T., Müller, R. D., Smith, W. H. F., Garcia, E., & Francis, R. (2014). New global marine gravity model from CryoSat-2 and Jason-1 reveals buried tectonic structure. *Science*, *346*(6205), 65–67. https://doi.org/10.1126/science.1258213

Schlindwein, V., Demuth, A., Korger, E., Läderach, C., & Schmid, F. (2015). Seismicity of the Arctic mid-ocean ridge system. *Polar Science*, *9*(1), 146–157. https://doi.org/10.1016/j.polar.2014.10.001

Schlindwein, V., & Schmid, F. (2016). Mid-ocean-ridge seismicity reveals extreme types of ocean lithosphere. *Nature*, *535*(7611), 276–279. https://doi.org/10.1038/nature18277

Schmidt-Aursch, M., & Haberland, C. (2017). DEPAS (Deutscher Geräte-Pool für amphibische Seismologie): German Instrument Pool for Amphibian Seismology. *Journal of largescale research facilities*, *3*, A122. https://doi.org/10.17815/jlsrf-3-165

Schneider, A., Panieri, G., Lepland, A., Consolaro, C., Crémière, A., Forwick, M., et al. (2018). Methane seepage at Vestnesa Ridge (NW Svalbard) since the last glacial maximum. *Quaternary Science Reviews*, *193*, 98–117. https://doi.org/10.1016/j.quascirev.2018.06.006

Schweitzer, J. (2001). HYPOSAT—An enhanced routine to locate seismic events. *Pure and Applied Geophysics*, *158*(1), 277–289. https://doi.org/10.1007/pl00001160

Singhroha, S., Bünz, S., Plaza-Faverola, A., & Chand, S. (2016). Gas hydrate and free gas detection using seismic quality factor estimates from high-resolution P-cable 3D seismic data. *Interpretation*, *4*(1), SA39–SA54. https://doi.org/10.1190/int-2015-0023.1

Singhroha, S., Bünz, S., Plaza-Faverola, A., & Chand, S. (2020). Detection of gas hydrates in faults using azimuthal seismic velocity analysis, Vestnesa Ridge, W-Svalbard Margin. *Journal of Geophysical Research: Solid Earth*, *125*(2), e2019JB017949. https://doi.org/10.1029/2019jb017949

Singhroha, S., Chand, S., & Bünz, S. (2019). Constraints on gas hydrate distribution and morphology in Vestnesa Ridge, Western Svalbard Margin, using multicomponent ocean-bottom seismic data. *Journal of Geophysical Research: Solid Earth*, *124*(5), 4343–4364. https://doi.org/10.1029/2018jb016574

Smith, A. J., Mienert, J., Bünz, S., & Greinert, J. (2014). Thermogenic methane injection via bubble transport into the upper Arctic Ocean from the hydrate-charged Vestnesa Ridge, Svalbard. *Geochemistry, Geophysics, Geosystems*, *15*(5), 1945–1959. https://doi.org/10.1002/2013gc005179

Solomon, S., Carpenter, M., & Flach, T. A. (2008). Intermediate storage of carbon dioxide in geological formations: A technical perspective. *International Journal of Greenhouse Gas Control*, *2*(4), 502–510. https://doi.org/10.1016/j.ijggc.2008.04.004

Steffen, H., Olesen, O., & Sutinen, R. (2021). *Glacially-triggered faulting*. Cambridge University Press.

Steffen, R., Steffen, H., Wu, P., & Eaton, D. W. (2014). Stress and fault parameters affecting fault slip magnitude and activation time during a glacial cycle. *Tectonics*, *33*(7), 1461–1476. https://doi.org/10.1002/2013tc003450

Sultan, N., Plaza-Faverola, A., Vadakkepuliyambatta, S., Buenz, S., & Knies, J. (2020). Impact of tides and sea-level on deep-sea Arctic methane emissions. *Nature Communications*, *11*(1), 5087. https://doi.org/10.1038/s41467-020-18899-3

Talwani, M., & Eldholm, O. (1977). Evolution of the Norwegian-Greenland sea. *GSA Bulletin*, *88*(7), 969–999. https://doi.org/10.1130/0016-7606(1977)88<969:eotns>2.0.co;2

Thorson, R. M. (2000). Glacial tectonics: A deeper perspective. *Quaternary Science Reviews*, *19*(14), 1391–1398. https://doi.org/10.1016/s0277-3791(00)00068-8

Vachon, R., Schmidt, P., Lund, B., Plaza-Faverola, A., Patton, H., & Hubbard, A. (2022). Glacially induced stress across the arctic from the Eemian interglacial to the present—Implications for faulting and methane seepage. *Journal of Geophysical Research: Solid Earth*, *127*(7). https://doi.org/10.1029/2022jb024272

Vanneste, M., Guidard, S., & Mienert, J. (2005). Bottom-simulating reflections and geothermal gradients across the western Svalbard margin. *Terra Nova*, *17*(6), 510–516. https://doi.org/10.1111/j.1365-3121.2005.00643.x

Vogt, P. R., Crane, K., Sundvor, E., Max, M. D., & Pfirman, S. L. (1994). Methane-generated( ) pockmarks on young, thickly sedimented oceanic crust in the Arctic. Vestnesa ridge, Fram strait. *Geology*, *22*(3), 255. https://doi.org/10.1130/0091-7613(1994)022<0255:mgpoyt>2.3.co;2

Waghorn, K. A., Vadakkepuliyambatta, S., Plaza-Faverola, A., Johnson, J. E., Bunz, S., & Waage, M. (2020). Crustal processes sustain Arctic abiotic gas hydrate and fluid flow systems. *Scientific Reports*, *10*(1), 10679. https://doi.org/10.1038/s41598-020-67426-3

Wessel, P., Luis, J. F., Uieda, L., Scharroo, R., Wobbe, F., Smith, W. H. F., & Tian, D. (2019). The generic mapping tools version 6. *Geochemistry, Geophysics, Geosystems*, *20*(11), 5556–5564. https://doi.org/10.1029/2019GC008515

Wiemer, S., & Wyss, M. (2000). Minimum magnitude of completeness in earthquake catalogs: Examples from Alaska, the western United States, and Japan. *Bulletin of the Seismological Society of America*, *90*(4), 859–869. https://doi.org/10.1785/0119990114

Wyss, M., Hasegawa, A., Wiemer, S., & Umino, N. (1999). Quantitative mapping of precursory seismic quiescence before the 1989, M 7.1 off-Sanriku earthquake, Japan. *Annals of Geophysics*, *42*(5). https://doi.org/10.4401/ag-3765

Zoback, M. L., Zoback, M. D., Adams, J., Assumpção, M., Bell, S., Bergman, E. A., et al. (1989). Global patterns of tectonic stress. *Nature*, *341*(6240), 291–298. https://doi.org/10.1038/341291a0